AIAA AVIATION Forum
5-9 June 2017, Denver, Colorado
23rd AIAA/CEAS Aeroacoustics Conference

Check for updates

Beamforming-Based Wavepacket Model for Noise Environment Predictions of Tactical Aircraft

Blaine M. Harker,[1] Kent L. Gee,[2] Tracianne B. Neilsen,[3]
Brigham Young University, Provo, UT, 84602

Alan T. Wall[4]
Air Force Research Laboratory, Wright-Patterson Air Force Base, OH, 45433

and

Michael M. James[5]
Blue Ridge Research and Consulting, LLC, Asheville, NC, 28801

Downloaded by BRIGHAM YOUNG UNIVERSITY on June 8, 2017 | http://arc.aiaa.org | DOI: 10.2514/6.2017-4048

Jet noise consists of extended, partially correlated sources such that a single-wavepacket source representation is inadequate. A multiple-wavepacket (MWP) model provides an analytical framework for jet-noise-like radiation to simulate jet noise field levels as well as the corresponding spatial coherence properties within the field. Here, a beamforming method with regularization is applied to noise measured by a linear array near a high-performance military aircraft. Beamforming results are decomposed into a reduced-order MWP model and the predicted radiation is validated in terms of level and coherence properties using benchmark measurements. Sound levels and coherence lengths generated by the beamforming results show good agreement with benchmark measurements over a range of frequencies that contribute significantly to the overall radiation. The MWP model is shown to predict full-scale specific features such as multilobe directivity patterns, and the addition of an uncorrelated distribution (UD) model adequately predicts the sideline radiation that is otherwise difficult to reproduce from wavepacket radiation. The MWP model predicted radiation characteristics are an improvement over single-wavepacket models, which do not incorporate spatiotemporal features of the radiation.

Nomenclature

a	=	amplitude of $\boldsymbol{q}_{\mathrm{wpkt}}$
a_{UD}	=	peak amplitude of $\boldsymbol{q}_{\mathrm{UD}}$
c_1	=	growth rate of Gaussian function in $\boldsymbol{q}_{\mathrm{wpkt}}$
c_2	=	decay rate of Gaussian function in $\boldsymbol{q}_{\mathrm{wpkt}}$
$\mathbf{C}$	=	cross-spectral matrix
$\boldsymbol{\mathcal{C}}$	=	wavepacket amplitude coefficients matrix
d	=	number of wavepackets in multiple-wavepacket model
D	=	jet nozzle diameter
f	=	frequency
$g(\vec{r}_i, \vec{r}_j)$	=	Green function response between positions $\vec{r}_i$ and $\vec{r}_j$
$\mathbf{G}$	=	Green function response matrix
$\mathbf{G}^{\dagger}$	=	Moore-Penrose pseudo-inverse of $\mathbf{G}$
$\boldsymbol{\mathcal{G}}$	=	matrix of steering vectors
i_{ref}	=	position index of signal reference location, $\vec{r}_{\mathrm{ref}}$
k	=	acoustic wavenumber

[1] Graduate Student, Dept. of Physics and Astronomy, N283 ESC, AIAA Student Member.
[2] Associate Professor, Dept. of Physics and Astronomy, N283 ESC, AIAA Senior Member.
[3] Part-Time Assistant Professor, Dept. of Physics and Astronomy, N283 ESC, AIAA Member.
[4] Research Physicist, Battlespace Acoustics Branch, AFRL 711 HPW/RHCB, AIAA Member.
[5] Senior Principal Engineer, 29 N Market St, Suite 700, AIAA Member.

Copyright © 2017 by B.M. Harker, K.L. Gee, T.B. Neilsen, A.T. Wall, and M.M. James. Published by the American Institute of Aeronautics and Astronautics, Inc., with permission.

k_{peak} = peak wavenumber of $\boldsymbol{q}_i$
ℓ = number of singular values used in determining MUSIC power
m = number of measurement array microphones
$\hat{p}_j$ = complex pressure measurement at $\vec{r}_j$
$\mathbf{p}$ = pressure measurements vector
$\mathbf{P}_f$ = partial field matrix
$\mathbf{P}_{\text{MUSIC}_i}$ = MUSIC power at $\vec{r}_i$
q_i = complex source strength at $\vec{r}_i$
$\mathbf{q}$ = complex source strengths vector
$\boldsymbol{q}_i$ = partial field of $\mathbf{Q}_z$
$\boldsymbol{q}_{\text{UD}}$ = uncorrelated source distribution vector
$\boldsymbol{q}_{\text{wpkt}}$ = asymmetric-Gaussian wavepacket function
$\mathbf{Q}_{\text{CBF}}$ = cross-spectral matrix of the source reconstruction from cross-beamforming results
$\mathbf{Q}_{\text{GINV}}$ = cross-spectral matrix of the source reconstruction from generalized inverse-beamforming results
$\mathbf{Q}_{\text{wpkt}}$ = unscaled source cross-spectral matrix from multiple-wavepacket model
$\mathbf{Q}_{\text{MWP/+UD}}$ = scaled source cross-spectral matrix from multiple-wavepacket model / with uncorrelated distribution
$\mathbf{Q}_z$ = iteration of cross-spectral source model in multiple-wavepacket decomposition
$\vec{r}_j$ = position vector at position index j
$\mathbf{R}$ = residual subspace matrix
s = number of potential source positions
$\mathbf{u}$ = trial vector for determining $\mathbf{P}_{\text{MUSIC}}$
$\mathbf{U}$ = unitary matrix from the decomposition of $\mathbf{G}$
$\boldsymbol{v}$ = vector of i_{ref}th row from $\mathbf{W}$
$\mathbf{V}$ = unitary matrix from the decomposition of $\mathbf{G}$
$\mathbf{w}$ = eigenvectors from $\mathbf{W}$
$\boldsymbol{w}$ = eigenvector of $\mathbf{Q}_z$ scaled by corresponding singular value
$\mathbf{W}$ = unitary matrix from eigendecomposition of $\mathbf{Q}_z$
$\boldsymbol{\mathcal{W}}$ = eigenvector matrix of $\mathbf{Q}_z$ scaled by corresponding singular values
z_i = spatial variable along source region and component of $\vec{r}_i$
$\gamma^2_{j_1 j_2}$ = coherence between measurements at $\vec{r}_{j_1}$ and $\vec{r}_{j_2}$
δ = regularization penalization parameter
ϵ_α = error at αth iteration of the uncorrelated distribution
λ = wavelength
$\mathbf{\Lambda}$ = diagonal matrix from eigendecomposition of $\mathbf{Q}_z$
$\mathbf{\Sigma}$ = diagonal matrix from the decomposition of $\mathbf{G}$

I. Introduction

Efforts to better understand and model the radiation of jet noise using wavepacket-like distributions have seen increased interest over the past decade.[1-5] Wavepacket models have been used in the description of acoustic, hydrodynamic, and turbulent features of jet noise.[5] However, because of the harsh environment and hot, fast flows in the vicinity of full-scale jet noise measurements, phased arrays are well-suited for full-scale applications to estimate properties of the source region without the need to measure the source directly.[6, 7] Beamforming methods can also be used to obtain equivalent source properties from limited array apertures for reliable source information.[8] However, there are method-specific assumptions in each particular beamforming algorithm that influence the calculated source characteristics. Various jet noise phased-array analyses have been conducted using conventional methods. Lee and Bridges[9] applied beamforming techniques to jet noise using a linear array about 15 nozzle diameters from and parallel to the jet centerline to reconstruct equivalent source distributions at the nozzle and along the jet axis. They showed the variation in the source dimensions was strongest for high frequency component noise originating near the nozzle exit when various nozzle geometries and mixers were interchanged. Papamoschou *et al.*[2] applied a beamforming method to far-field pressure measurements to calculate the correlation with flow-field measurements along the jet shear layer. They found non-negligible correlation between the acoustic measurements and the turbulent flow field.

Because jet noise sources are generally noncompact and partially correlated in nature,[10] more advanced beamforming methods have been proposed to address potential discrepancies arising from the traditional beamforming assumptions.[11] For instance, Venkatesh *et al.*[12] as well as Schlinker *et al.*[6] utilized beamforming methods that weighted

Downloaded by BRIGHAM YOUNG UNIVERSITY on June 8, 2017 | http://arc.aiaa.org | DOI: 10.2514/6.2017-4048

the measurements to account for the distributed nature of the source, but without explicitly considering source correlation. Several methods have since been developed that account for source correlation, many of which involve cross beamforming. Brooks and Humphreys[13] developed the deconvolution approach for the mapping of acoustic sources (DAMAS), and then extended the DAMAS algorithm to allow for correlated and partially correlated sources (DAMAS-C), although at a relatively high computational cost.[14] These deconvolution techniques allow for the removal of the array point-spread function, thus improving spatial resolution and source level estimates. Some methods have circumvented the beamforming map to solve a cost function for source distributions that match the measured microphone array levels.[15, 16] Michel and Funke[15] developed the source directivity modeling of a cross-spectral matrix (SODIX) to model jet engine noise as a linear source distribution along the jet centerline where each source distribution element had an associated directivity, and their source models were able to correctly predict the far-field radiation benchmarks and to spatially separate the inlet, cowling and jet noise contributions in the radiation predictions. Regularized inverse techniques have also been introduced in conjunction with cross-beamforming algorithms that allow for source correlation, including the hybrid method[17] and generalized inverse beamforming (GINV).[11, 18] These methods provide a more simplistic and computationally efficient means to solve for the source distributions, and while they can be used in conjunction with the deconvolution approaches, the advanced beamforming methods need not necessarily utilize deconvolution to improve results. The results from these methods generate a full-order source cross-spectral matrix that can be used as an equivalent source model of the jet noise.

Wavepacket models provide a reduced-order, analytical and physical framework for modeling the beamforming results. They are defined as advecting disturbances that are correlated over distances exceeding the integral scales of turbulence and have been used to describe the Mach wave radiation of supersonic jet noise[5, 16] as well as for subsonic noise.[4] Suzuki and Colonius[1] modeled the instability waves of near field subsonic jet noise using an eigenfunction approach to beamforming. Kœnig *et al*[4] decomposed far-field noise measurements of a subsonic cold laboratory jet using an orthogonal decomposition of the pressure field into a single modal component, which they compared to the radiation of a wavepacket model. Du and Morris[19] applied conventional beamforming to simulated far-field jet noise data to obtain the acoustic complex pressure at the jet lipline, which was then decomposed using a wavepacket model for Strouhal numbers of 0.3 and 0.6. When compared to the simulated far field pressure measurements, the estimated pressure field from the first wavepacket mode showed general agreement. Reba *et al.*[3] measured the hydrodynamic pressure field and fit the amplitude and correlation measurements to Gaussian-shaped wavepackets of the first two azimuthal modes. When used to predict acoustic levels, each wavepacket model showed good agreement with acoustic measurements in the peak radiation region. In building upon the studies in which the levels of the field have been shown to be reasonably reproduced using a single wavepacket ansatz, in this paper, the modeling of the source correlation properties is accomplished using a combination of wavepacket components, each with a different amplitude distribution and wavenumber. A multiple-wavepacket (MWP) model provides a more complete estimate of the jet noise environment by broadening the directionality of the acoustic radiation and by providing a field that has spatially dependent, finite coherence lengths.

In this paper, a multiple-wavepacket source model of the noise radiation from a high-performance tactical aircraft is developed using beamforming results at the jet centerline, and the resultant frequency-dependent equivalent source distribution is useful to predict both the levels and spatiotemporal properties of the corresponding radiation. An improved generalized-inverse beamforming method[11] that includes regularization is described in Section II. However, the beamforming results are generally given in an inefficient, nonintuitive way that requires the full matrix solution to adequately describe the source reconstruction. A method to decompose the matrix solution into a concise model, consisting of a minimal number of wavepackets identified by a few parameters, is desired. This reduced-order source model can be used to describe the resultant radiation of the field both in terms of level[3] and coherence properties[20]. In previous work,[4, 16] it was shown that one wavepacket per frequency could adequately describe the far-field levels for lower frequencies and in the peak radiation direction. However, as was recently shown,[21] the coherence properties of the field require multiple partially coherent sources to capture the finite coherence lengths. A broadband MWP model of the beamforming results predicts the radiated level and coherence properties, and the method is applied to jet noise data from a tactical aircraft at three engine powers to produce a complex, extended source reconstruction in Section III. The beamforming result and the MWP model are validated using benchmark jet noise measurements in the mid field, and it is shown that the reduced order models provide a simplified analytical framework with which to capture the salient radiation features as well as the more intricate properties observed in full-scale jet noise measurements. The models also provide physical insight into the source characteristics as they vary with frequency and engine condition.

Downloaded by BRIGHAM YOUNG UNIVERSITY on June 8, 2017 | http://arc.aiaa.org | DOI: 10.2514/6.2017-4048

II. Methods

The process of using a beamforming-based approach to model jet noise to create a reduced-order model is described. First, pressure measurements from a microphone array near an acoustic source are inserted into an advanced beamforming method with regularization, and the beamforming results produce an equivalent source model. This beamforming-based source model is used to create a reduced-order MWP model, which provides a simplified analytical framework and allows for extensions to other similar-typed sources. The MWP model is then used to predict the levels and coherence properties of the acoustic field.

Unlike traditional far-field beamforming methods where the source-to-array distance is much larger than the array dimensions, beamforming in the geometric near field can lead to improved resolution.[13] However, the level of improvement is determined by the choice of reconstruction locations, the array geometry and dimensions relative to the source size, and the frequency under consideration. In this study, the array design is chosen to be sufficiently dense to produce high-resolution estimates of the source distribution without the need for deconvolution methods. In addition, the array spans the source region such that resolution across the source region is approximately uniform, although additional complications can arise from more directional sources. In this study, cross beamforming is briefly described, which is a precursor to improved generalized inverse beamforming[11] that will be applied in this paper. The GINV beamforming results create an equivalent source model that is decomposed into a reduced-order MWP model, and the method for determining the multiple wavepackets is detailed.

A. Cross Beamforming

Cross beamforming is an extension of traditional beamforming that can identify source coherence characteristics. An array consisting of m microphones is used to measure the pressure field, $\hat{p}_j$, at each array element location, $\vec{r}_j$, where $j = 1 \dots m$. The measurement is made at a given frequency, f, which is not explicitly referenced for convenience. Considering potential sources located at positions $\vec{r}_i$, each with a complex source strength of q_i, where $i = 1 \dots s$, the acoustic pressure measured at $\vec{r}_j$ can be described as

$$\hat{p}_j = g(\vec{r}_i, \vec{r}_j) q_i. \tag{1}$$

Here, the free-field Green function, $g(\vec{r}_i, \vec{r}_j)$, incorporates the propagation from the source to the measurement location. There will be m equations that can conveniently be rewritten in matrix format, such that

$$\mathbf{p} = \mathbf{G}\,\mathbf{q}, \tag{2}$$

where the vector of acoustic pressures, $\mathbf{p}$, is $[m, 1]$ in length and the vector of complex source strengths, $\mathbf{q}$, is $[s, 1]$. The Green function matrix, $\mathbf{G}$, is $[m, s]$ in size and accounts for the free-field propagation from each volume velocity source to each array element. We seek to solve for $\mathbf{q}$, which is accomplished by solving a similar inverse problem:

$$\mathbf{q} = \boldsymbol{\mathcal{G}}^{\mathrm{H}}\mathbf{p}, \tag{3}$$

where H is the conjugate transpose operator. The operator, $\boldsymbol{\mathcal{G}}^{\mathrm{H}}$, is the steering vector matrix that can be formulated in several ways. In the traditional matrix beamforming methods, $\boldsymbol{\mathcal{G}}^{\mathrm{H}} = \mathbf{G}^{\mathrm{H}}$.[22] As an alternative approach, various steering vector methods have been proposed that are designed to enhance various aspects of source characteristics.[23] Sarradj[23] compares four common steering vector formulations and each is shown to either correctly reproduce the source level or the source location. In the present study, the fourth steering vector definition is used, which Sarradj showed to produce the source location and to slightly underpredict the source level. The resulting cross beamforming (CBF) response follows as an outer product of the source strengths vector,

$$\mathbf{Q}_{\mathrm{CBF}} = \mathbf{q}\mathbf{q}^{\mathrm{H}} = \mathbf{G}^{\mathrm{H}}\mathbf{p}\mathbf{p}^{\mathrm{H}}\mathbf{G} = \mathbf{G}^{\mathrm{H}}\mathbf{C}\mathbf{G}, \tag{4}$$

where the quantity $\mathbf{C} \equiv \mathbf{p}\mathbf{p}^{\mathrm{H}}$ is the cross-spectral matrix corresponding to the acoustic measurements. $\mathbf{Q}_{\mathrm{CBF}}$ is a cross-spectral matrix of the source reconstruction estimated by the cross beamforming, and diagonal elements of $\mathbf{Q}_{\mathrm{CBF}}$ contain the individual source powers commonly reported in conventional beamforming. The off-diagonal elements, $\mathbf{Q}_{\mathrm{CBF}_{i_1,i_2}}$, where i_1 and i_2 are the indices of $\mathbf{Q}_{\mathrm{CBF}}$ and correspond to source locations $\vec{r}_{i_1}$ and $\vec{r}_{i_2}$, are referred to as the cross beamforming elements and represent the simultaneous steering of the array pressures to two locations along the source region. The magnitude of the estimated cross beamforming response relative to the corresponding individual source responses, $\mathbf{Q}_{\mathrm{CBF}_{i_1,i_1}}$ and $\mathbf{Q}_{\mathrm{CBF}_{i_2,i_2}}$, is large if there exists a degree of coherence between corresponding source locations. Techniques, such as DAMAS-C, rely on the cross beamforming response to model sources that exhibit

Downloaded by BRIGHAM YOUNG UNIVERSITY on June 8, 2017 | http://arc.aiaa.org | DOI: 10.2514/6.2017-4048

some degree of mutual coherence but also apply a deconvolution technique to account for array artifacts [14]. In this instance, the array geometry was such that the addition of deconvolution should not improve the source resolution.

B. Generalized Inverse Beamforming

The improved generalized inverse beamforming method described by Dougherty[11] is distinct from cross beamforming in one primary point. As opposed to using a Green function for cross beamforming to calculate the steering vector matrix in Eq. (4), the improved generalized inverse method uses the Moore-Penrose generalized inverse of the steering vector matrix, $\mathbf{G}^{\dagger}$ [11]. This is a more direct method for solving Eq. (2) and in practice can be calculated by taking the inverse of the singular value decomposition of $\mathbf{G}$ (where the decomposition is $\mathbf{G} = \mathbf{U}\,\mathbf{\Sigma}\,\mathbf{V^H}$). The inverse is then simply calculated by taking the inverse of the diagonal singular values matrix, $\mathbf{\Sigma}$. The result of the generalized inverse method is then

$$\begin{aligned}\mathbf{Q}_{\mathrm{GINV}} &= \mathbf{G}^{\dagger}\,\mathbf{C}\,(\mathbf{G}^{\dagger})^{\mathrm{H}} \\ &= \mathbf{V}\,\mathbf{\Sigma^{-1}}\mathbf{U}^{\mathrm{H}}\,\mathbf{C}\,\mathbf{U}\,\mathbf{\Sigma^{-1}}\mathbf{V}^{\mathrm{H}},\end{aligned} \tag{5}$$

Because very small singular values are amplified by the inversion, regularization is necessary to determine an appropriate lower limit in the singular values. All values below this limit are replaced with a lower limiting value to bound the amplification of less-pertinent features of the Green function matrix. The choice of cutoff levels can significantly alter the resultant field predictions, particularly in the low-level radiation regions. To allow for a smooth source estimate as well as a smooth field estimate that does not contain additional spurious artifacts, a cutoff value of 1.4 dB below the largest singular value was chosen, similar the choice empirically chosen by Dougherty.[11]

C. Wavepacket Source Model

The GINV beamforming results produce a full-order matrix solution of the original sources, and when describing a distributed, partially correlated source, the number of elements in $\mathbf{Q}_{\mathrm{GINV}}$ is s^2, which can be large and is often excessive. However, previous studies have shown the effectiveness of an analytical wavepacket model that spans multiple source positions, $\vec{r}_i$, to efficiently predict jet noise levels within the dominant radiation lobe.[4, 16, 19] A single wavepacket model, however, produces infinite coherence in describing both the source and corresponding radiation—contrary to the observed finite coherence lengths. The ability for a model to reproduce the spatiotemporal features of the field, e.g. coherence, requires a more complex model, and an analytical MWP model provides the capability to describe the finite coherence lengths present both in the source model, as well as for the radiated field. The process to generate the multiple wavepackets is described. The GINV beamforming results are decomposed into an MWP model through an iterative process and the analytical wavepackets are projected onto the beamforming results to extract each wavepacket's amplitude and phase contribution.

The multiple wavepacket source model is created in a multiple step iterative process. Each step is summarized in Fig. 1, and an explanation of each step follows.

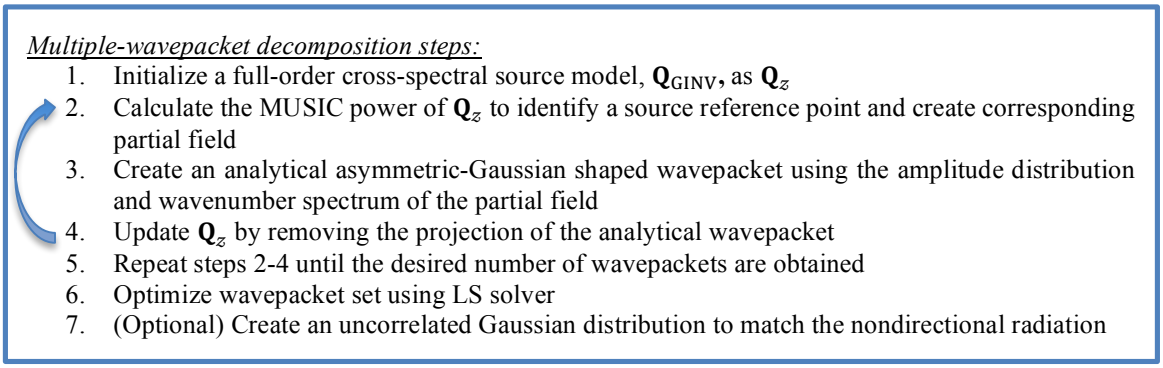

Fig. 1 Multiple wavepacket model creation process.

1. Initialization

The wavepacket decomposition process is initialized using the results of the beamforming algorithm, $\mathbf{Q}_{\mathrm{GINV}}$, which are set as the current cross-spectral source model, $\mathbf{Q}_z$. In this manner, $\mathbf{Q}_{\mathrm{GINV}}$ is treated as a full order model, and the goal of the wavepacket decomposition is to produce a reduced order model.

Downloaded by BRIGHAM YOUNG UNIVERSITY on June 8, 2017 | http://arc.aiaa.org | DOI: 10.2514/6.2017-4048

2. Calculate MUSIC power

The process of decomposing $\mathbf{Q}_z$ into a system of wavepackets is done iteratively, extracting one wavepacket at a time. First, the MUSIC power is applied to $\mathbf{Q}_z$ to identify a source location. A summary of the MUSIC algorithm is presented here, and additional information is found in Ref. [24, 25]. The noise subspace of $\mathbf{Q}_z$ is calculated using an eigendecomposition, such that

$$\mathbf{Q}_z = \mathbf{W}\,\mathbf{\Lambda}\,\mathbf{W}^{\mathrm{H}}, \tag{6}$$

where the unitary matrix, $\mathbf{W}$, is the set of singular vectors, and $\mathbf{\Lambda}$ is a diagonal matrix with the singular values comprising the diagonal. The singular vector matrix can be written $\mathbf{W} = [\mathbf{w}_1, \mathbf{w}_2, \ldots, \mathbf{w}_s]$, where $\mathbf{w}_p$ are the singular vectors. A signal subspace of $\mathbf{Q}_z$ is defined by assuming the first ℓ singular vectors span the space. The corresponding residual subspace is then formed by defining

$$\mathbf{R} = \sum_{p=\ell+1}^{s} \mathbf{w}_p \mathbf{w}_p^{\mathrm{H}}. \tag{7}$$

Here, ℓ is set to one so that only the space spanned by the largest singular vector is considered.

The goal of the MUSIC algorithm is to determine the spatial distribution of the equivalent source that contains the largest percentage of coherent field energy. This is accomplished indirectly by searching for a spatial position that contributes least to the residual subspace, $\mathbf{R}$. A trial vector $\mathbf{u}_i$, representing a trial source location at $\vec{r}_i$, is assumed such that $\mathbf{u}_i = [0 \ldots 0\ 1\ 0 \ldots 0]^{\mathrm{T}}$, with the vector having a value of one at index i. The MUSIC power is then defined as

$$\mathbf{P}_{\mathbf{MUSIC}_i} = \frac{1}{\mathbf{u}_i^{\mathrm{H}}\,\mathbf{R}\,\mathbf{u}_i}. \tag{8}$$

Note that if the trial vector is equivalent to a singular vector in the signal subspace, $\mathbf{P}_{\mathbf{MUSIC}_i} \to \infty$. The MUSIC power estimates the most likely source position as the highest value of $\mathbf{P}_{\mathbf{MUSIC}_i}$, and the index i_{ref}, corresponding location at $r_{i_{\mathrm{ref}}}$, is chosen as the signal reference location.

Using the source reference location, $r_{i_{\mathrm{ref}}}$, a partial field is extracted from $\mathbf{Q}_z$. The i_{ref}th row of $\mathbf{W}$ is chosen, corresponding to the i_{ref}th element of each singular vector as $\boldsymbol{v} = \left[\mathbf{w}_{1,i_{\mathrm{ref}}}, \mathbf{w}_{2,i_{\mathrm{ref}}} \ldots \mathbf{w}_{s,i_{\mathrm{ref}}}\right]$. This vector is multiplied by $\mathbf{W}$ and scaled by the i_{ref}th diagonal element of $\mathbf{Q}_z$. The cross-product of $\boldsymbol{v}$ and the singular vector matrix, when scaled by the corresponding source level, extracts a partial field, $\boldsymbol{q}$, from $\mathbf{Q}_z$, such that

$$\boldsymbol{q} = \frac{\mathbf{W} \cdot \boldsymbol{v}^{\mathrm{H}}}{\sqrt{\mathbf{Q}_{z_{i_{\mathrm{ref}},i_{\mathrm{ref}}}}}}. \tag{9}$$

This partial field is an [s,1] vector comprised of the portion of $\mathbf{Q}_z$ that exhibits coherence with a source located at $r_{i_{\mathrm{ref}}}$. If only a single source located at $r_{i_{\mathrm{ref}}}$ were present and the measurement was noiseless, then $\boldsymbol{q}\boldsymbol{q}^{\mathrm{H}}$ would be equivalent to $\mathbf{Q}_z$. Conversely, if high levels of additional signals and/or noise contributed to $\mathbf{Q}_z$, then $\boldsymbol{q}$ would only contain a portion of the energy of $\mathbf{Q}_z$.

3. Create analytical asymmetric-Gaussian shaped wavepacket

The extracted partial field, $\boldsymbol{q}$, is an empirically-determined equivalent source derived from the beamforming results that can be used to create a corresponding analytical wavepacket. If the potential sources locations are distributed linearly, the shape of $\boldsymbol{q}$, in many cases, has similarities with that of an asymmetric-Gaussian function—which are related to underlying wavepacket-like source properties[5]—with the functional form,

Downloaded by BRIGHAM YOUNG UNIVERSITY on June 8, 2017 | http://arc.aiaa.org | DOI: 10.2514/6.2017-4048

$$\boldsymbol{q}_{\mathrm{wpkt}}(z) = \begin{cases} a\exp\left(-\dfrac{2\ln 2\left(z - z_{i_{\mathrm{ref}}}\right)^2}{c_1^2} + j\left(k_{\mathrm{peak}}z\right)\right), & z < z_{i_{\mathrm{ref}}} \\ a\exp\left(-\dfrac{2\ln 2\left(z - z_{i_{\mathrm{ref}}}\right)^2}{c_2^2} + j\left(k_{\mathrm{peak}}z\right)\right), & z \geq z_{i_{\mathrm{ref}}} \end{cases}. \tag{10}$$

The analytical function has a, c_1 and c_2 that are determined by the partial field amplitude, the growth rate and the decay rate, respectively. Equation (10) is a function of the spatial variable, z, along the source region and $z_{i_{\mathrm{ref}}}$ is the component of $r_{i_{\mathrm{ref}}}$ along the source distribution dimension. The amplitude is set such that the peak of the magnitude of $\boldsymbol{q}_{\mathrm{wpkt}}(z_{i_{\mathrm{ref}}})$ is unity. Because the wavepacket is asymmetric, the growth rate, c_1, is an 'equivalent' measure of the full-width half maximum value. It is obtained by doubling the width from the peak at $z_{i_{\mathrm{ref}}}$ to the closest location in the $-z$ direction from the peak at which the amplitude is half of the maximum. The decay rate, c_2, for the second part of the wavepacket is obtained in similar fashion, except the width is measured from $z_{i_{\mathrm{ref}}}$ to the location in the $+z$ direction at which the amplitude is half of the maximum. The wavepacket function is also complex, and the complex argument is dependent on the peak wavenumber, k_{peak}, of the partial field's corresponding wavenumber spectrum. The wavenumber spectrum of the partial field is obtained by taking a discrete spatial Fourier transform of $\boldsymbol{q}$. The wavenumber corresponding to the maximum value of the spectrum determines k_{peak}. The wavepacket fitting process provides an analytical representation that requires a minimal number of parameters.

4. Update $\mathbf{Q}_z$ by removing projection of the analytical wavepacket

While the analytical wavepacket is representative of the corresponding partial field, it only contains a portion of its energy and radiative properties, and the extent that the wavepacket models $\mathbf{Q}_z$ is unclear. A Graham-Schmidt process[26] is therefore performed using the eigenvectors of $\mathbf{Q}_z$ and $\boldsymbol{q}_{\mathrm{wpkt}}$ to obtain the span of $\boldsymbol{q}_{\mathrm{wpkt}}$ and the corresponding residual, which will be used to update $\mathbf{Q}_z$. The current cross-spectral source model is decomposed as

$$\begin{aligned} \mathbf{Q}_z = \mathbf{W}\,\boldsymbol{\Lambda}\,\mathbf{W}^{\mathrm{H}} &= \left(\mathbf{W}\,\boldsymbol{\Lambda}^{\frac{1}{2}}\right)\left(\boldsymbol{\Lambda}^{\frac{1}{2}}\,\mathbf{W}^{\mathrm{H}}\right) \\ &= \left(\mathbf{W}\,\boldsymbol{\Lambda}^{\frac{1}{2}}\right)\left(\mathbf{W}\;\boldsymbol{\Lambda}^{\frac{1}{2}}\right)^{\mathrm{H}} \\ &= \boldsymbol{\mathcal{W}}\,\boldsymbol{\mathcal{W}}^{\mathrm{H}} \end{aligned} \tag{11}$$

where singular values, σ_p are used to scale the singular vectors of $\mathbf{Q}_z$, to create a set of scaled singular vectors such that $\boldsymbol{w}_p = \sqrt{\boldsymbol{\sigma}_p}\,\mathbf{w}_p$. A Graham Schmidt process is carried out on each of the scaled singular vectors,

$$\boldsymbol{w}_{p,\mathrm{rem}} = \boldsymbol{w}_p - \frac{\boldsymbol{q}_{\mathrm{wpkt}}^{\mathrm{H}}\boldsymbol{w}_p}{\boldsymbol{q}_{\mathrm{wpkt}}^{\mathrm{H}}\boldsymbol{q}_{\mathrm{wpkt}}}\boldsymbol{q}_{\mathrm{wpkt}}. \tag{12}$$

This is done for each of the scaled singular vectors. The remainder vectors are combined into a matrix, $\boldsymbol{\mathcal{W}}_{\mathrm{rem}} = [\boldsymbol{w}_{1,\mathrm{rem}}, \boldsymbol{w}_{2,\mathrm{rem}}, \ldots \boldsymbol{w}_{s,\mathrm{rem}}]$, and a remainder matrix of $\mathbf{Q}_z$ is obtained,

$$\mathbf{Q}_{z,\mathrm{rem}} = \boldsymbol{\mathcal{W}}_{\mathrm{rem}}\boldsymbol{\mathcal{W}}_{\mathrm{rem}}^{\mathrm{H}}. \tag{13}$$

The Graham-Schmidt process removes the projection of the wavepacket from the current cross-spectral source model, and a new cross-spectral model is obtained.

5. Repeat to obtain desired number of wavepackets

The process of obtaining an additional analytical wavepacket is repeated by setting $\mathbf{Q}_{z+1} = \mathbf{Q}_{z,\mathrm{rem}}$ and proceeding from a recalculation of the MUSIC power. The required number of wavepackets for a given reduced order model is dependent on the number of sources present. For jet noise, the source spans many meters and many coherence lengths, dependent on the frequency of interest. A discussion on the adequate number of wavepackets is provided for jet noise measurements in Section III(E).

Downloaded by BRIGHAM YOUNG UNIVERSITY on June 8, 2017 | http://arc.aiaa.org | DOI: 10.2514/6.2017-4048

6. Optimize set of wavepackets using an LS solver

The wavepacket analytical functions provide a representative physical foundation for the observed acoustic radiation from jet noise. However, because the Gaussian-shaped wavepackets only approximately model their corresponding partial fields, the derived wavepacket set does not produce an orthogonal wavepacket basis. To best optimize the wavepacket set and assign amplitudes to each wavepacket, an optimization problem is cast as a linear set of equations, with the d wavepackets forming the columns of a wavepacket matrix, $\mathbf{Q}_{\text{wpkt}} = \left[\boldsymbol{q}_{\text{wpkt},1}, \boldsymbol{q}_{\text{wpkt},2} \cdots \boldsymbol{q}_{\text{wpkt},d}\right]$. The solution to

$$\mathbf{Q}_{\text{wpkt}}\, \boldsymbol{\mathcal{C}} = \boldsymbol{\mathcal{W}}_0, \tag{14}$$

is desired, where $\boldsymbol{\mathcal{W}}_0$ corresponds to the solution for the first iteration of Eq. (11), and $\boldsymbol{\mathcal{C}}$ is a $[d, s]$ coefficients matrix containing the contributions of each analytical wavepacket to describe the scaled singular vectors. If the number of singular values comprising the signal space of $\boldsymbol{\mathcal{W}}_0$ is known, fewer than s vectors can be used in Eq. (14) as appropriate. The solution to Eq. (14) is obtained using a Moore-Penrose pseudoinverse,[11] and Tikhonov regularization is also applied to ensure stability.[17] The solution is

$$\boldsymbol{\mathcal{C}} = \left(\mathbf{Q}_{\text{wpkt}}^{\text{H}}\mathbf{Q}_{\text{wpkt}} + \delta\mathbf{I}\right)^{-1}\mathbf{Q}_{\text{wpkt}}^{\text{H}}\boldsymbol{\mathcal{W}}_0. \tag{15}$$

The identity matrix, **I**, is scaled by a penalization parameter, δ, which can be determined using the Morozov discrepancy procedure or the generalized cross validation procedure.[27] Having determined the coefficients describing the analytical wavepacket contributions, the reduced order scaled singular vectors are

$$\boldsymbol{\mathcal{W}}_{\text{red}} = \left[\mathbf{Q}_{\text{wpkt}}\, \boldsymbol{c}_1, \mathbf{Q}_{\text{wpkt}}\, \boldsymbol{c}_2, \ldots, \mathbf{Q}_{\text{wpkt}}\, \boldsymbol{c}_s\right], \tag{16}$$

where the coefficients vector, $\boldsymbol{c}_p$, is the pth column of $\boldsymbol{\mathcal{C}}$ and describes the contribution of each wavepacket to $\boldsymbol{w}_p$. The reduced order MWP model is then calculated as

$$\mathbf{Q}_{\text{MWP}} = \boldsymbol{\mathcal{W}}_{\text{red}}\boldsymbol{\mathcal{W}}_{\text{red}}^{\text{H}}. \tag{17}$$

The reduced order MWP model is a source cross-spectral matrix like the beamforming results, $\mathbf{Q}_{\text{GINV}}$, and can be treated like its full-order counterpart to predict the levels and coherence properties of the source and radiated field. The MWP model provides an analytical framework that decomposes the full-order results of $\mathbf{Q}_{\text{GINV}}$ to only the parameters that describe the wavepackets. In addition, the model methodology provides flexibility where multiple wavepackets are necessary to adequately reproduce the full-order model results, especially as the frequency is varied. It also provides a for connection of the models across frequency using the individual wavepackets, although a broadband MWP model is not treated in this present study.

7. Create uncorrelated Gaussian distribution to match the nondirectional radiation

The reduced order, MWP model characterizes the dominant wavepacket-like radiation contained in the beamforming equivalent source model. In many cases, additional radiation is also present which is not wavepacket like in its radiation and, therefore, is more difficult to model using solely wavepacket contributions. In the case of jet noise radiation, sideline radiation is typically described as the product of fine-scale structure radiation, which is described as omnidirectional radiation from multiple uncorrelated sources.[10] The addition of an uncorrelated distribution can be used to augment the MWP model to produce radiation in a similar manner as seen in the radiation.

Starting from Eq. (10), the uncorrelated distribution (UD) is assumed to be shaped as a symmetric Gaussian function ($c_{1,\text{UD}} = c_{2,\text{UD}}$) with $k_{\text{peak}} = 0$ and centered at $b_{\text{UD}} = z_{i_{\max}}$, where $z_{i_{\max}}$ is the location along the beamforming source distribution corresponding to the maximum amplitude of the beamforming results. The full-width half maximum of the distribution is defined as three wavelengths, which was empirically determined to produce radiation that balances spherical and cylindrical spreading.

The amplitude of the distribution is determined by matching the original levels at the measurement array, **p**, to those predicted by the MWP model and the additional UD model in an iterative process. Starting with a distribution, $\boldsymbol{q}_{\text{UD}}$, the amplitude of the UD model is initialized at unity. This distribution is added to the MWP model by placing the squared elements of the distribution along a diagonal matrix to create a cross-spectral matrix of the uncorrelated distribution with off-diagonal elements set to zero. This produces the MWP+UD model as

Downloaded by BRIGHAM YOUNG UNIVERSITY on June 8, 2017 | http://arc.aiaa.org | DOI: 10.2514/6.2017-4048

$$\mathbf{Q}_{\mathrm{MWP+UD}} = \mathbf{Q}_{\mathrm{MWP}} + \mathrm{Diag}\left[\boldsymbol{q}_{\mathrm{UD}}^{\mathbf{2}}\right]. \tag{18}$$

The MWP+UD model is used to predict the levels at the original measurement array as $\mathbf{p}_{\mathrm{pred}}$, and the process for predicting the levels is described in Section D. The error between $\mathbf{p}_{\mathrm{pred}}$ and $\mathbf{p}$ is calculated for a subsection of the measurement region where the MWP model underpredicts the levels, e.g. perpendicular to the jet at the sideline where fine-scale structure radiation is the primary contributor. The error is calculated at the αth iteration as

$$\epsilon_{\alpha} = \frac{1}{r}\sum_{j=1}^{r}\left(\frac{\left|\mathbf{p}_{\mathrm{pred},j}\right|}{\left|\mathbf{p}_{j}\right|} - 1\right), \tag{19}$$

where the predicted and measured levels at the subset of r measurement locations determine the amplitude adjustment parameter, ϵ_{α}. The distribution amplitude, a_{UD} is then updated,

$$a_{\mathrm{UD},\alpha+1} = a_{\mathrm{UD},\alpha}(\epsilon_{\alpha} - 1). \tag{20}$$

A new $\boldsymbol{q}_{\mathrm{UD}}$ is calculated and the process is repeated until $\mathbf{p}_{\mathrm{pred}}$ converges on $\mathbf{p}$ to determine a_{UD}. The uncorrelated distribution provides the omnidirectional radiation and limited coherence properties that are otherwise difficult to model using solely wavepackets.

D. Field Predictions

Where source benchmarks are not available, the ability of the source model to predict field characteristics determines the models effectiveness and reliability. The source model, $\mathbf{Q}$, is propagated for each of the methods by defining a new Green function, $\mathbf{G}_a$, that includes steering vectors for additional locations [11]. The cross spectral matrix of field pressures, $\mathbf{C}_a$, at the desired locations can by modeled using

$$\mathbf{C}_a = |\mathbf{G}_a\mathbf{q}|^2 = \mathbf{G}_a\,\mathbf{Q}\,\mathbf{G}_a^{\mathbf{H}}. \tag{21}$$

Levels are calculated by taking the magnitude the diagonal elements of $\mathbf{C}_a$ and converted to a decibel scale. Furthermore, $\mathbf{C}_a$ provides the necessary information to calculate the coherence properties of the field. For reference location, $\vec{r}_{j_1}$, and another position $\vec{r}_{j_2}$, the coherence is calculated as

$$\gamma_{j_1,j_2}^2 = \frac{\left|\mathbf{C}_{a\,j_1,j_2}\right|^2}{\mathbf{C}_{a\,j_1,j_1}\mathbf{C}_{a\,j_2,j_2}}. \tag{22}$$

Because coherence is dependent on a reference location,[28] coherence lengths provide a means of summarizing the spatial variation in the coherence.[29] Coherence length is defined as the distance from a reference location over which coherence is significant ($\gamma^2 \geq 0.5$). The ability of MWP equivalent source models obtained from beamforming methods to predict coherence lengths is an important measure of the methods' success when applied to an extended, partially correlated source.

III. Results

The methods described in Section II are applied to analyze measurements taken from a full-scale turbofan engine. Generalized inverse beamforming is applied to measurements taken at a linear array to produce a full-order beamforming source model in Section B. The MWP decomposition technique is applied to the beamforming measurements in Section C and the MWP model is analyzed. In Section D, the beamforming source model and MWP model are used to predict radiation levels at the scan array and measurement arc, and the results are compared with the benchmark measurements. In addition, the coherence measured along a linear array is compared to predictions from the beamforming and MWP models. The predicted radiation of the MWP model is analyzed to show that key radiation features are well-represented. In Section E, the required number of wavepackets in the MWP model is analyzed to adequately represent radiation level and coherence properties. Section F extends the WMP model analysis to include additional engine power configurations, showing the changes in the radiation properties as well as the requirements and resultant changes of the MWP model.

A. Experiment

Downloaded by BRIGHAM YOUNG UNIVERSITY on June 8, 2017 | http://arc.aiaa.org | DOI: 10.2514/6.2017-4048

Noise measurements were collected in the vicinity of an installed, full-scale turbofan engine at four engine conditions ranging from idle to afterburner. A planar microphone array arranged in an 18 x 5 rectangular grid pattern with 15.24 cm inter-element spacing was moved to multiple locations shown by triangles in Fig. 2(a). In this paper, only the microphones closest to the ground (0.38 m) are used from each planar array measurement, and they are referred to as the scanning array, located 5.6 m from and parallel to the estimated shear layer. The same planar array, when placed at polar angles in the mid field between 90° and 148° (relative to the nozzle inlet) is referred to as the measurement arc. Each planar array measurement is collected at a radial distance of 22.86 m from the microphone array reference position, located 5.5 m downstream of the nozzle exit. The measurement arc is comprised of measurements from a single row of microphones, located at a height of 1.60 m, that are taken from each planar array measurement. A separate 50-microphone ground-based array recorded measurements simultaneously, for reference, during each planar microphone array measurement. As shown in Fig. 2(a), the ground array element spacing is 0.61 m, and the array spans 30 m. A detailed description of the experiment is found in Ref. [30].

The one-third octave levels at the ground-based array are shown in Fig. 2(b) for MIL engine condition (100% engine thrust request [ETR]). The MIL condition is used in the analyses of Sections B-E, and Section F revisits the methods and procedures for additional engine conditions. At this engine condition, two primary radiation lobes are present in the ground array data, centered at $z = 15$ m and 250 Hz and $z = 20$ m and 125 Hz. These radiation lobes extend many meters spatially as well as across multiple third-octave measurements. A more detailed analysis of the spectral variation of the measured sound as a function of angle is provided in Ref. [31]. While jet-nozzle exit conditions are not available, a prior study estimated an appropriate frequency-to-Strouhal-number scaling of approximately $1.2 \cdot 10^{-3}$ Hz^{-1} such that the octave frequency range reported in this paper is approximately $0.04 \leq Sr \leq 0.4$.

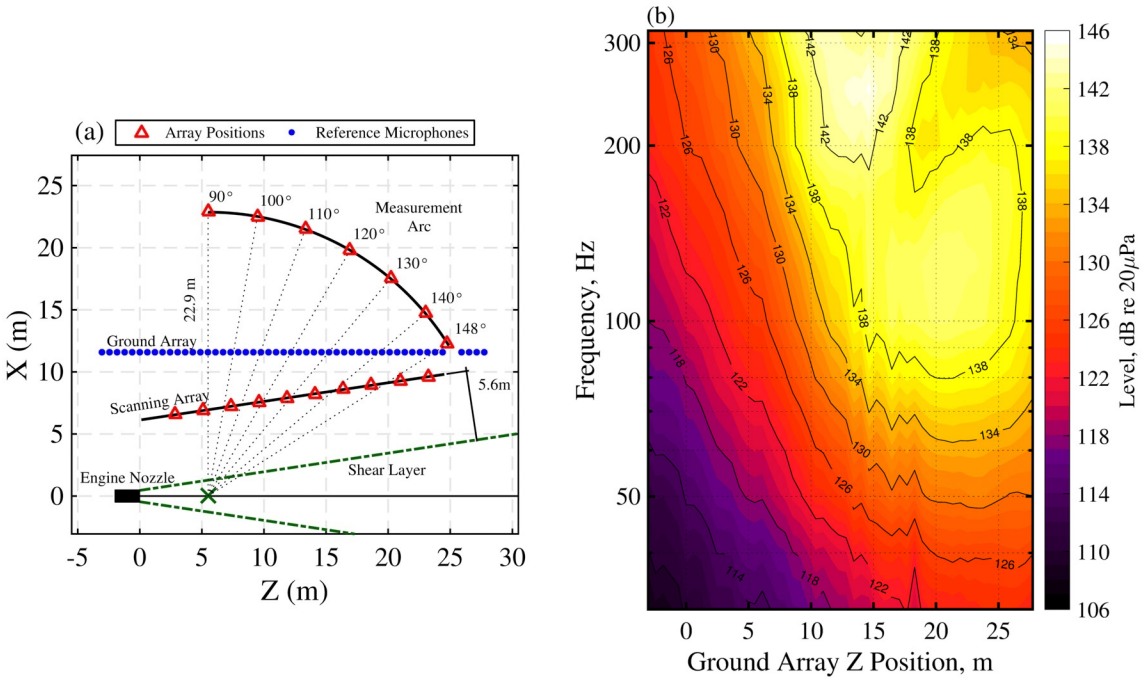

Fig. 2. (Left) Schematic of the experimental setup. Red triangle locations represent measurement positions of the 90-microphone planar array, and a ground-based array of 50 microphones are shown with blue dots. (Right) The one-third octave band levels at MIL engine condition along the ground array are shown.

B. Beamforming Results

Beamforming methods were applied to the ground-based array measurements shown in Fig. 2 to obtain beamforming equivalent source strength results along the jet centerline. The one-third-octave center-frequency beamforming results are shown in Fig. 3(a), which have been scaled by the bandwidth. The results show a strong distributed source region that peaks in amplitude at for frequencies above 100 Hz and that extends beyond 315 Hz (beyond the spatial Nyquist frequency of the array). Liu *et al.*[32] use LES simulations to show that for very heated jets the acoustic pressure levels at the jet lipline are affected by the radiation efficiency and turbulent kinetic energy corresponding to a given

Downloaded by BRIGHAM YOUNG UNIVERSITY on June 8, 2017 | http://arc.aiaa.org | DOI: 10.2514/6.2017-4048

frequency. They showed that for simulations of a heated jet simulating afterburner conditions with jet velocity of Mach 1.5, frequencies that correspond to subsonic convective phase speeds ($Sr \leq 0.1$) radiated inefficiently, while higher frequencies radiated with more efficient supersonic convective speeds. In addition, the axial pressure distribution along the lipline was greatest for $0.04 \leq Sr \leq 0.3$, and the combined observations contribute to the far-field radiation levels, which were greatest for $0.1 \leq Sr \leq 0.3$. The frequencies over which the peak levels are present both in the beamforming results as well as for radiated levels agree support the observations by Liu *et al.*

The beamforming results are also plotted relative to the respective maximum level in Fig. 3(b) to more clearly show the beamforming source distribution for each band. The source region extends many meters downstream of the nozzle (located at $z = 0$ m) with the peak locations marked by the black asterisks. A common report of prior beamforming studies of jet noise—including those using LES-simulations,[33] laboratory[8, 9] and full-scale experiments[6, 7]—is the gradual decrease in source size as well as the upstream-shifting peak level location with increasing frequency. The contraction in source size here agrees with previous findings and, as measured in Fig. 3(b) using the 3 dB down contour lines, the source distribution reduces from 14 m at 32 Hz to 4.0 m at 315 Hz. When adjusted by wavelength, however, the source distribution increases steadily from 1.3λ at 32 Hz to 3.6λ at 315 Hz. This is qualitatively consistent with measurements from Schlinker *et al.,*[6] who found that for an uninstalled full-scale supersonic exhaust stream engine, the source width—measured using beamforming results using the 3 dB down points from the maximum level—nearly doubled in width from 250 Hz to 500 Hz when scaled by wavelength. While the peak level location, $z_{peak}(f)$, shifts towards the nozzle with increasing frequency, when scaled by wavelength this distance increases gradually from $z_{peak}(32\text{ Hz}) = 0.6\lambda$ to $z_{peak}(125\text{ Hz}) = 2.0\lambda$ and even more pronounced for higher frequencies with $z_{peak}(315\text{ Hz}) = 3.4\lambda$. Lee and Bridges[34] found that for a heated supersonic jet ($D = 2$ in., $M_a = 1.57$, TR $= 2.7$), the peak beamforming levels ranged from $z_{peak}(Sr = .04) = 13\ z/D$ to $z_{peak}(Sr = 0.4) = 7\ z/D$, which are consistent with results for the present engine condition.

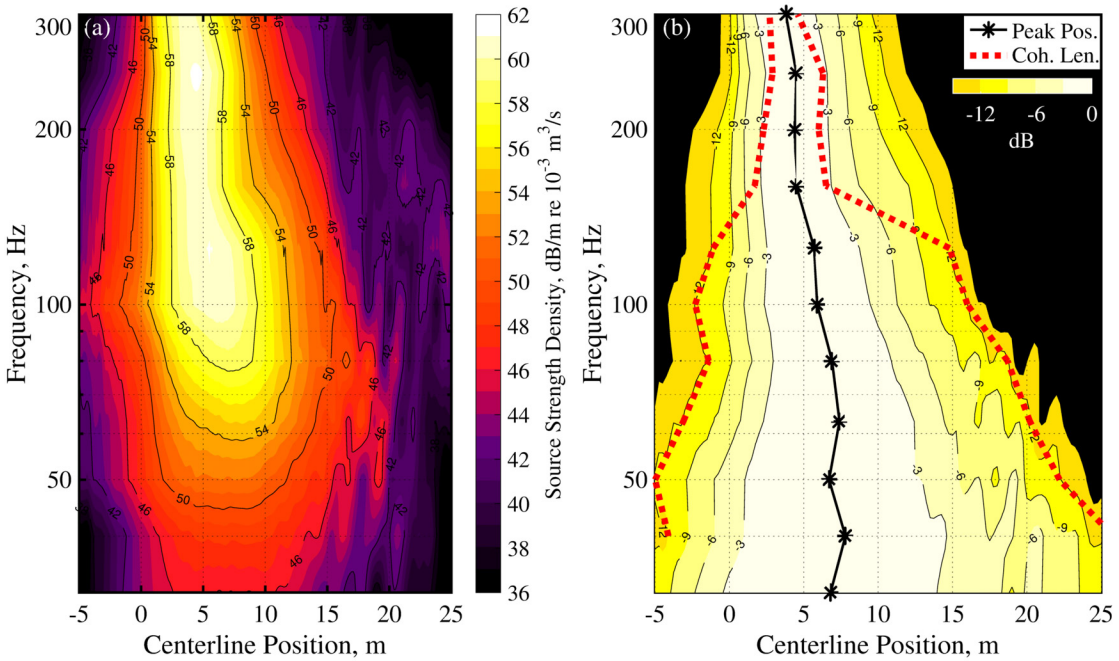

Fig. 3. Beamforming results at jet centerline shown (a) in absolute levels and (b) relative to the maximum level of each one-third octave band. The location of the maximum level at each frequency is indicated with an asterisk, and the coherence region over which coherence exceeds 0.5 relative to the peak beamforming level location is also delineated with a red dashed line.

The coherence of the beamforming results is also measured using Eq. (22) and replacing $\boldsymbol{C_p}$ for $\boldsymbol{Q}$, referenced to the peak level location. The locations in which coherence drops below 0.5, as measured relative to the frequency-dependent peak beamforming level locations, are marked by red dashed lines in Fig. 3(b). The distance between these coherence lines for a given frequency is hereafter referred to as the coherence length. Coherence lengths at frequencies

Downloaded by BRIGHAM YOUNG UNIVERSITY on June 8, 2017 | http://arc.aiaa.org | DOI: 10.2514/6.2017-4048

below 160 Hz are on the order 3-6 wavelengths [coinciding with the 12 dB down lines of the beamforming results in Fig. 3(b)], with coherence lengths increasing with frequency (with respect to wavelength). However, coherence lengths above 160 Hz are only about two wavelengths in length. The source coherence length as well as source size and peak level location suggest a transition region separating phenomenological distinctions in the source characteristics. This transition region has appeared in other studies as well. Stout *et al.*[35] noted a dramatic shift between 150-250 Hz in the estimated source location using an vector intensity-based approach. The source region shifted from 5-8 m to 3-5 m in this transition region. Wall *et al.*[36] show a split in the reconstructed equivalent source distribution in this region using an advanced acoustical holography technique. The peak source level location also shifts from about 7 m to about 5 m downstream. Above 160 Hz, the increased source size (in terms of wavelength) and decrease in coherence length suggest that multiple partially-correlated sources are required to appropriately model the source distribution.

C. Wavepacket Decompositions

From the equivalent beamforming-based source reconstructions in Fig. 3, MWP source models are developed for six wavepackets using the techniques described in Section II. The decomposed MWP models are shown in Fig. 4(a-c) for 315, 160 and 80 Hz, which represent above, in, and below the transition region in the beamforming source results. The beamforming levels are shown as a solid black line, with the MWP overall level shown in a gray dotted line, and the six individual wavepackets are shown as dashed color lines. The combined level of the MWP model shows good agreement with the beamforming model over the majority of the beamforming levels, although the low-level beamforming levels are not represented by the MWP model. In some instances, an individual wavepacket level will exceed the overall levels that results from coherent addition of the wavepackets and the ensuing potential for constructive and destructive interferences. Thus, the magnitude of each individual wavepacket contribution is not necessarily summed to get the overall levels.

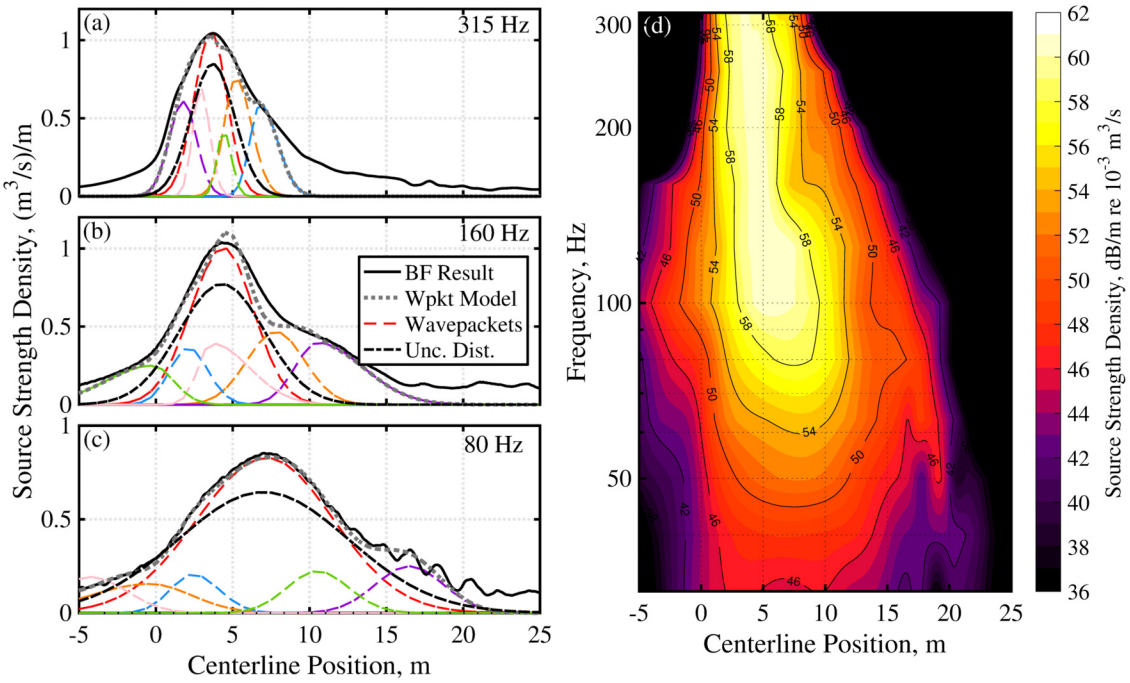

Fig. 4 Wavepacket examples at (a) 315 Hz, (b) 160 Hz, and (c) 80 Hz using six wavepackets are shown with the beamforming and resultant wavepacket model levels. An uncorrelated distribution is also plotted alongside each result. (d) Overall levels of the beamforming-based wavepacket source models are shown along jet centerline.

In addition to the MWP source model, an uncorrelated distribution is also used to augment the reduced order MWP model, as shown by a dash-dot line. Reduced order models have been shown by Papamoschou[16] and by Koenig *et al.*[4] to be particularly effective in describing the Mach wave radiation in far-field predictions, although they suffer

Downloaded by BRIGHAM YOUNG UNIVERSITY on June 8, 2017 | http://arc.aiaa.org | DOI: 10.2514/6.2017-4048

particularly in describing the sideline radiation. To compensate, Papamoschou included an additional monopole source to boost the sideline radiation. The uncorrelated distribution levels are determined in an iterative process to match the MWP levels plus the uncorrelated distribution to the levels measured along the sideline ($-2\text{ m} \leq z \leq 5\text{ m}$). Because the uncorrelated nature of this distribution, the radiation adds only incoherently as a function of frequency, instead of coherently for the wavepackets. Thus, the relative level of the uncorrelated distribution may be on the order of or higher amplitude than the overall MWP levels if there is significant uncorrelated radiation.

The combined overall levels of the MWP models are shown in Fig. 4(d) for each of the one-third-octave center frequencies, with the wavepacket model at each frequency represented using six wavepackets. The use of fewer or more wavepackets for the MWP source model is explored in Section E. The results show a strong similarity with the beamforming results in Fig. 3(a), particularly for levels which are within the top 12 dB of the peak level for each frequency. Levels below this, however, are underpredicted by the MWP model, including regions far upstream or downstream of the main source region. This may not necessarily be problematic, as the low-level beamforming results are typically less consequential and the physical interpretation of levels below the top 12 dB stand to be questioned. However, the addition of more wavepackets beyond the six per frequency employed continue to add to the model until they converge to the beamforming results.

D. Estimated Field Levels and Coherence

An equivalent source model of the jet noise radiation provides for the estimation of level and coherence information of the radiation field and provides an efficient means of characterizing the radiation. To validate the beamforming-based equivalent source model (hereafter referred to as beamforming source model) and the MWP source model previously described, the estimated levels at the ground array, the scan array and the measurement arc are considered. These are propagated from the source models as described in Section II(0), and the source model is reflected about the ground to produce the ground reflection to create the interference patterns present at the scan array and measurement arc. In addition, the uncorrelated Gaussian distribution is used to augment the wavepacket model. Measurements at the ground array, the scan array and the measurement arc are compared to the estimated levels by the three methods at 80 Hz, 160 Hz and 315 Hz in Fig. 5. In each plot the measurements at each array are represented by black triangles, and the predicted levels from the beamforming source model are shown by red squares. The orange stars and purple circles represent the predicted levels from the MWP model and MWP model with an uncorrelated distribution (MWP+UD model), respectively. The estimated levels from the beamforming source model and the MWP model show good agreement at all three measurement locations, within two dB in most locations for both frequencies. The notable exception is in the estimated levels of the MWP model to estimate the sideline levels, which underestimate the sideline measurement levels by as much as 15 dB or more. The sideline levels are best represented using the measurements from the ground array, which extends up to about 4.5 m farther upstream than the scan array and about 7 m farther than the measurement arc. The addition of the uncorrelated distribution in the MWP+UD model boosts the sideline levels such that they are within measurement levels to within 2 dB throughout. There is also evidence of multilobe directivity patterns at 160 Hz and 315 Hz, particularly at the scan array.

Downloaded by BRIGHAM YOUNG UNIVERSITY on June 8, 2017 | http://arc.aiaa.org | DOI: 10.2514/6.2017-4048

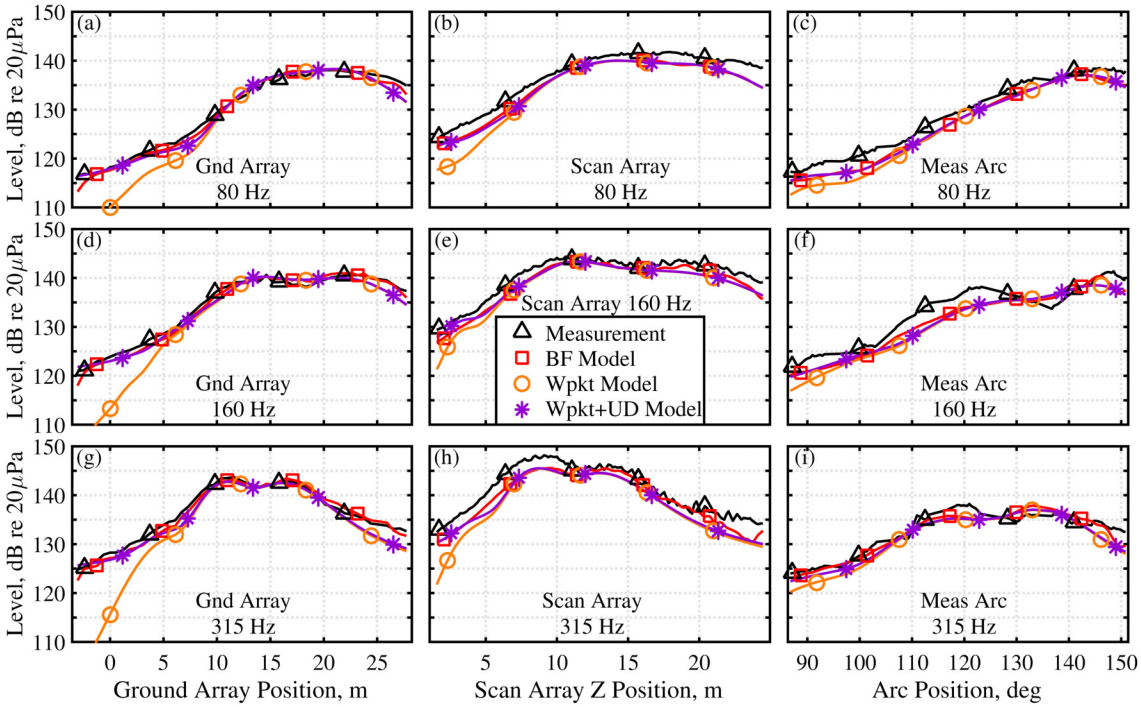

Fig. 5. Comparisons of measurements and predicted levels for (a-c) 80 Hz and (d-f) 160 Hz at (left) the ground array, (middle) the scan array, and (right) the measurement arc. The predictions are made using a beamforming source model, a multiple-wavepacket source model, and a multiple-wavepacket model with an additional distributed uncorrelated source.

The capabilities of the beamforming model and wavepacket model to estimate the field levels extend beyond the 80 Hz, 160 Hz and 315 Hz examples, shown in Fig. 5. The one-third octave center-frequency spectra from 32 Hz to 315 Hz at the measurement arc are shown in Fig. 6(a). In addition, the estimated levels using the MWP model and the MWP+UD model are given in Fig. 6(b-c), respectively, and the errors of these estimated levels when compared to measurements are given in Fig. 6(d-e). The measurements show two strong radiation lobes, one centered about 145° at 125 Hz, and the other centered at about 125° at 250 Hz. The size and frequency bandwidth of these two lobes considerable, expanding many degrees in either direction and spanning multiple third-octave bands. The multilobe features seen at 160 Hz in Fig. 5(f) are more apparent here and seem to be formed from contributions of both lobes. In the radiation from both MWP and MWP+UD models, the key features of the radiation are present.

As shown in Fig. 6(d-e), the predicted levels using the MWP model show agreement with the measurements to within about 2 dB over most the measurement arc and across the frequency bandwidth, with notable exceptions at upstream locations. At 63 Hz and at 250 Hz, errors more than 6 dB are present at about the 105° location, suggesting that six wavepackets do not sufficiently predict the radiation for these frequencies and an additional wavepacket may significantly reduce the present errors. In addition, the errors to the sideline range from 1-8 dB owing to the difficulty of wavepackets to predict sideline radiation. The addition of the uncorrelated distribution in the MWP+UD model significantly boosts the sideline levels so that the errors are reduced to about 1-2 dB.

Downloaded by BRIGHAM YOUNG UNIVERSITY on June 8, 2017 | http://arc.aiaa.org | DOI: 10.2514/6.2017-4048

Downloaded by BRIGHAM YOUNG UNIVERSITY on June 8, 2017 | http://arc.aiaa.org | DOI: 10.2514/6.2017-4048

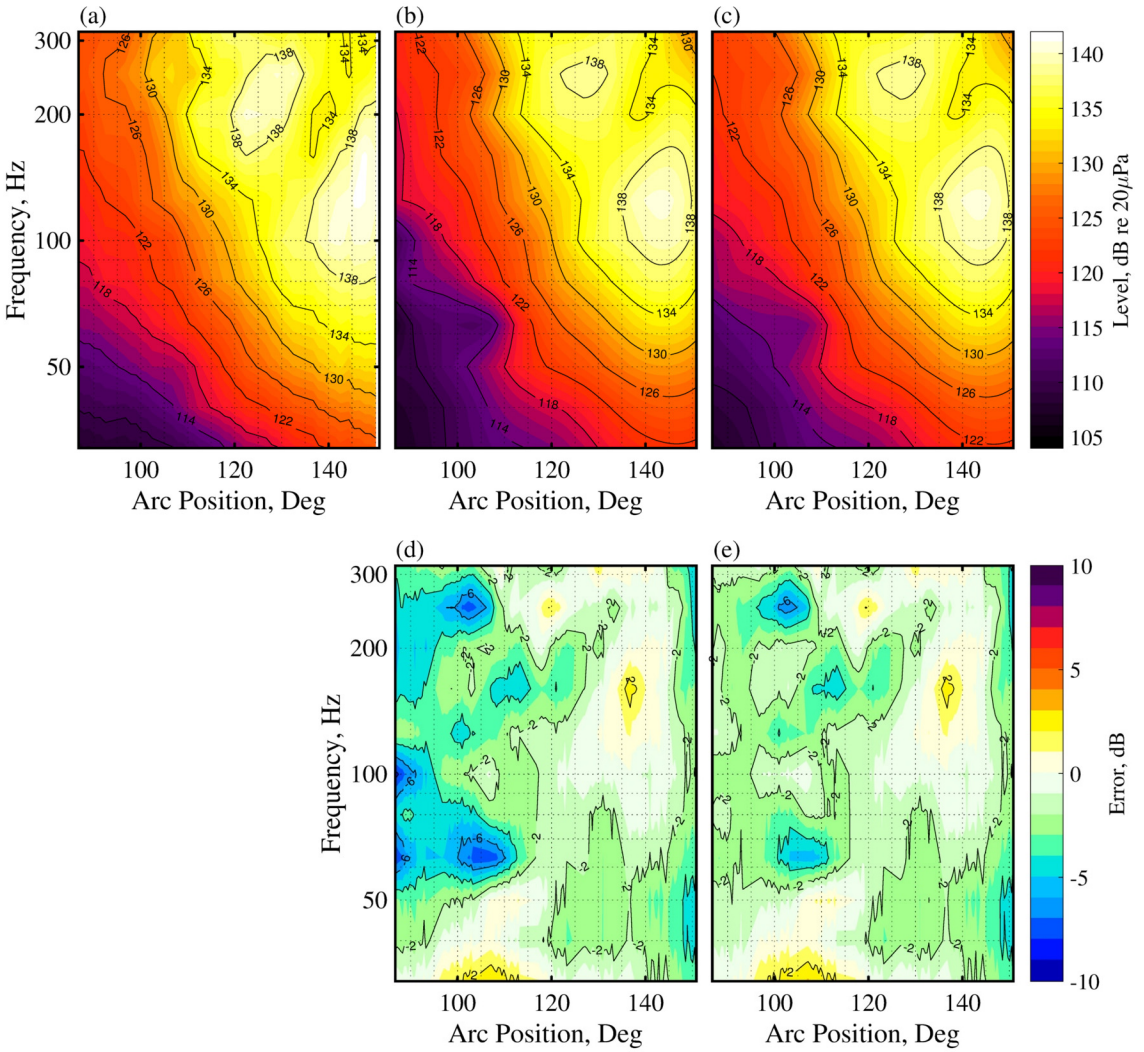

Fig. 6. (a) Level measurements at measurement arc, and predicted levels from (b) wavepacket source model and (c) wavepacket and uncorrelated distribution source model. The errors of the estimated levels to measurements for (d) the wavepacket model and (e) the wavepacket and uncorrelated distribution model are also given.

The beamforming model, MWP model, and MWP+UD model, having been validated in the available measurement regions shown in Fig. 5, are used to estimate the acoustic radiation near the jet at 80 Hz, 160 Hz and 315 Hz in Fig. 7. Each of the source models is based on ground-based array measurements, so the estimated levels are only assumed to be accurate for radiation contained within the white dashed lines. The lines coincide with the approximate aperture of the ground-based array and the jet centerline at 0 m for the upstream line and 20 m for the downstream, approximating the source region of the jet noise sources. This is only an approximate region of certainty, as the jet noise sources vary greatly in directionality with respect to source position and frequency. The field is propagated along the ground plane to better visualize the radiation without the inclusions of constructive and destructive interferences. The results show that all three methods produce similar fields in the maximum radiation regions, which highlights their consistency and the capabilities of the reduced order model to reproduce the full-order beamforming model. At 160 Hz and 315 Hz, the multilobe directivity patterns of the jet noise is apparent. The primary deviation between the models lies in the sideline radiation of the MWP model, which significantly underpredicts the levels produced by the beamforming model. The MWP+UD model boosts the levels at the sideline to those like the beamforming results. Wall *et al.*[21] used acoustical holography to predict the radiated levels for the current test conditions. They showed that while the levels for holography were reconstructed at a height of 1.9 m and ground interference patterns were present in the results, the radiation lobes show agreement in directivity and in terms of level, after accounting for the increase of pressure

for ground level predictions. They found that with increasing frequency, the relative levels between the multilobe features changed such that the levels of the more upstream lobe increased with frequency, while the levels of the lobe radiating farther downstream decreased.

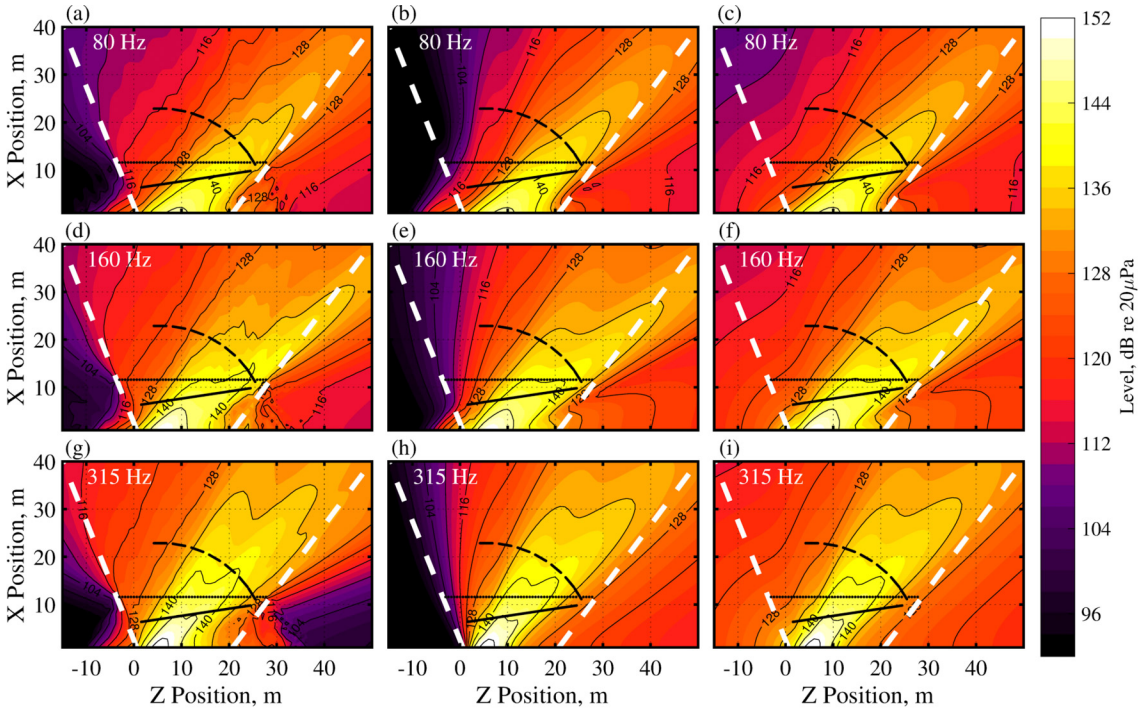

Fig. 7. Predicted levels across a horizontal plane with jet centerline on Z axis. Cases for (a-c) 80 Hz, (d-f) 160 Hz, and (g-h) 315 Hz are shown using (left) a beamforming source model, (middle) a multiple-wavepacket source model, and (right) a multiple-wavepacket model with an additional monopole distribution. The white-dashed lines represent the approximate aperture spanned by the ground-based array.

Because of the directive radiation produced from a wavepacket source, the multilobe features seen in the measurements in Fig. 6 are well represented using the multiple-wavepacket model, as well as the for the predicted levels in the vicinity of the jet shown in Fig. 7. Each wavepacket in the MWP model is associated with a wavenumber, derived from the wavenumber spectrum of its associated partial field, and the wavenumber produces radiation with a specific directivity. By viewing the individual contributions of the wavepackets, the reproduction of the multilobe phenomenon is better understood, and field level predictions from each of the multiple-wavepacket model at 160 Hz are plotted in Fig. 8. In this example, the first few wavepackets contribute most to the multilobe radiation. The first wavepacket radiates at an angle of about 139° to produce the primary lobe. The second wavepacket comprises the secondary lobe with a directivity of 121°.The third wavepacket is a lower-amplitude variation of the first wavepacket, with a slightly more downstream radiation angle of 143°. Wall *et al.*[21] found that, for 200 Hz, the radiation was reducible into two partial fields, plus a residual. If we consider only the first and second wavepackets, their result is corroborated by this reduction, and the remaining wavepackets are necessary to reconstruct any residual energy of the two lobes, as well as upstream and downstream lower-level contributions. Wall *et al.* also concluded that the coherence between the radiation of the two lobes was low and suggested that two overlapping yet mutually incoherent partial sources were responsible for the radiation, each of which having a characteristic phase speed. The MWP source model provides evidence that overlapping sources with differing phase speeds could indeed generate multilobe radiation patterns.

Downloaded by BRIGHAM YOUNG UNIVERSITY on June 8, 2017 | http://arc.aiaa.org | DOI: 10.2514/6.2017-4048

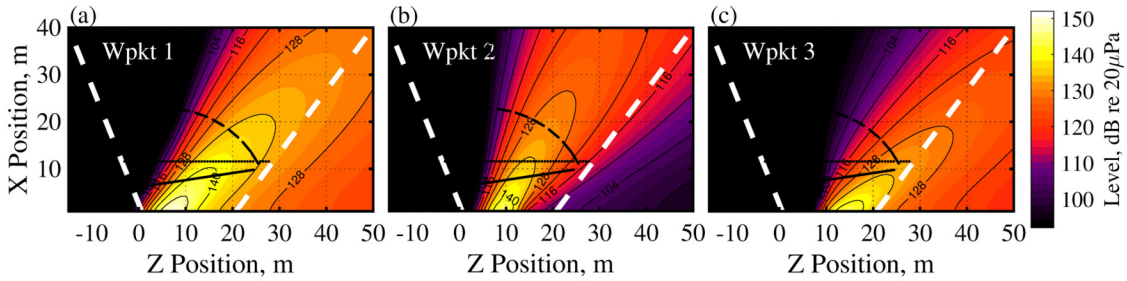

Fig. 8. Individual wavepacket contributions of the multiple-wavepacket model at 160 Hz.

In many cases, the primary wavepacket constitutes most of the radiated acoustic energy, particularly for frequencies below about 125 Hz. A comparison of the first wavepacket shapes, when normalized and scaled by wavelength, are shown in Fig. 9. Each primary wavepacket spans multiple wavelengths (corresponding to several meters) and, when scaled by wavelength, the wavepackets share are only slightly asymmetric in shape. This agrees with findings by Reba *et al.,*[37] who used radiation from a single Gaussian-shaped wavepacket to model pressure measurements near the shear-layer of a supersonic jet. They noted that the correlation length scales of the wavepacket source extended several nozzle diameters. When scaled by wavelength, the wavepackets in Fig. 9 grow in width with frequency, up to about 50 Hz. Between 50-80 Hz, the wavepackets continue to grow with frequency but only marginally and mainly along the decaying tail of the wavepacket. And beyond 80 Hz the scaled primary wavepackets show appreciable self-consistency with a wavepacket width of 2.5±0.3 wavelengths measured at the full-width half maximum. This is surprising considering that the beamforming results of the source distribution from Fig. 3(b)—when scaled by wavelength—show that the source width nearly triples over the same frequency bandwidth. This result suggests that the relative importance of the nonprimary wavepackets increases with frequency and that the combination of these wavepackets, when spatially distributed, comprise the source distribution. It is also interesting to note that the fluctuation of the coherence lengths with frequency, while varying in Fig. 3(b) between 2-6 wavelengths, does not seem to affect the individual wavepacket sizes.

The directivities of each wavepacket are also provided in the legend of Fig. 9. They show that the directivity of the first wavepacket steadily shifts from 129° to 139° as frequency increases from 32 Hz to about 160 Hz. Thereafter a transition occurs and the directivity of the primary wavepacket shifts to angles closer to the sideline. The trend then continues and the directivity shifts downstream from 123° to 130° from 200 Hz to 315 Hz. This transition in directivity between 160 Hz and 200 Hz shows the shift in relative energy between the downstream and upstream radiation lobes, and it makes clear the subtler trend that with increasing frequency the directivity of each of the multilobe radiation features shifts downstream. The transition in directivity between multilobe radiation features, as well as the trend of the radiation to larger angles with increasing frequency is also shown by Wall *et al.*[38] in the predicted radiation from an F-35 at MIL power using an advanced near-field acoustical holography technique.

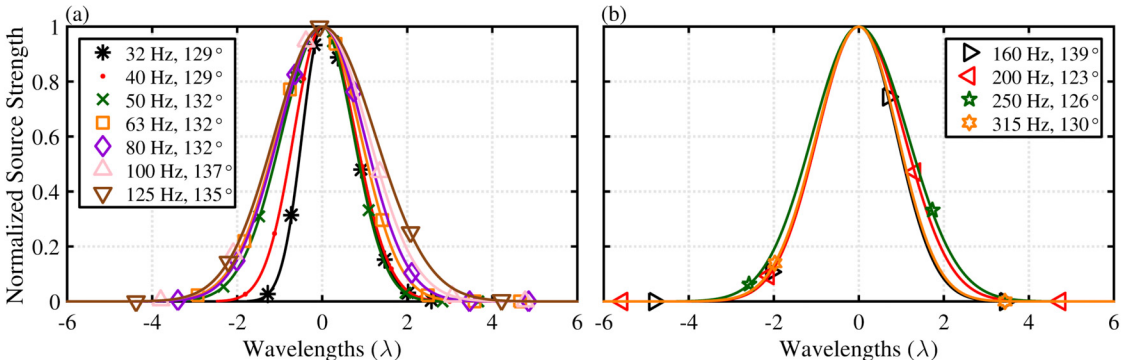

Fig. 9. Primary wavepacket shape that have been normalized and scaled by wavelength for one-third octave center frequencies.

Whereas a single wavepacket model fails to correctly reproduce the coherence properties of the acoustic radiation and struggles to reproduce radiation at all angles, the MWP model produces a field with finite coherence properties. Ground array coherence measurements were used to compare the predicted coherence properties of the field using the MWP and MWP+UD source models. The results of the measured and predicted coherence at 80, 160 and 315 Hz are

Downloaded by BRIGHAM YOUNG UNIVERSITY on June 8, 2017 | http://arc.aiaa.org | DOI: 10.2514/6.2017-4048

shown in Fig. 10. Coherence is shown such that the self-coherence for each plot is shown along the diagonal, with a value of unity, and the off-diagonal elements represent coherence between two corresponding measurement locations along the ground array. The coherence lengths are generally largest in the region where the direction of maximum radiation traverses the ground array, at about $Z = 10 - 25$ m downstream. At 80 Hz, the measured coherence lengths are greatest in the maximum radiation region [see Fig. 2(b)]. At 160 Hz, however, the multilobe radiation produces two spatial regions over which there is high coherence and a neck in the coherence map between the regions. The coherence is much lower across the array at 315 Hz, with coherence lengths in the maximum radiation region not exceeding 2-3 m.

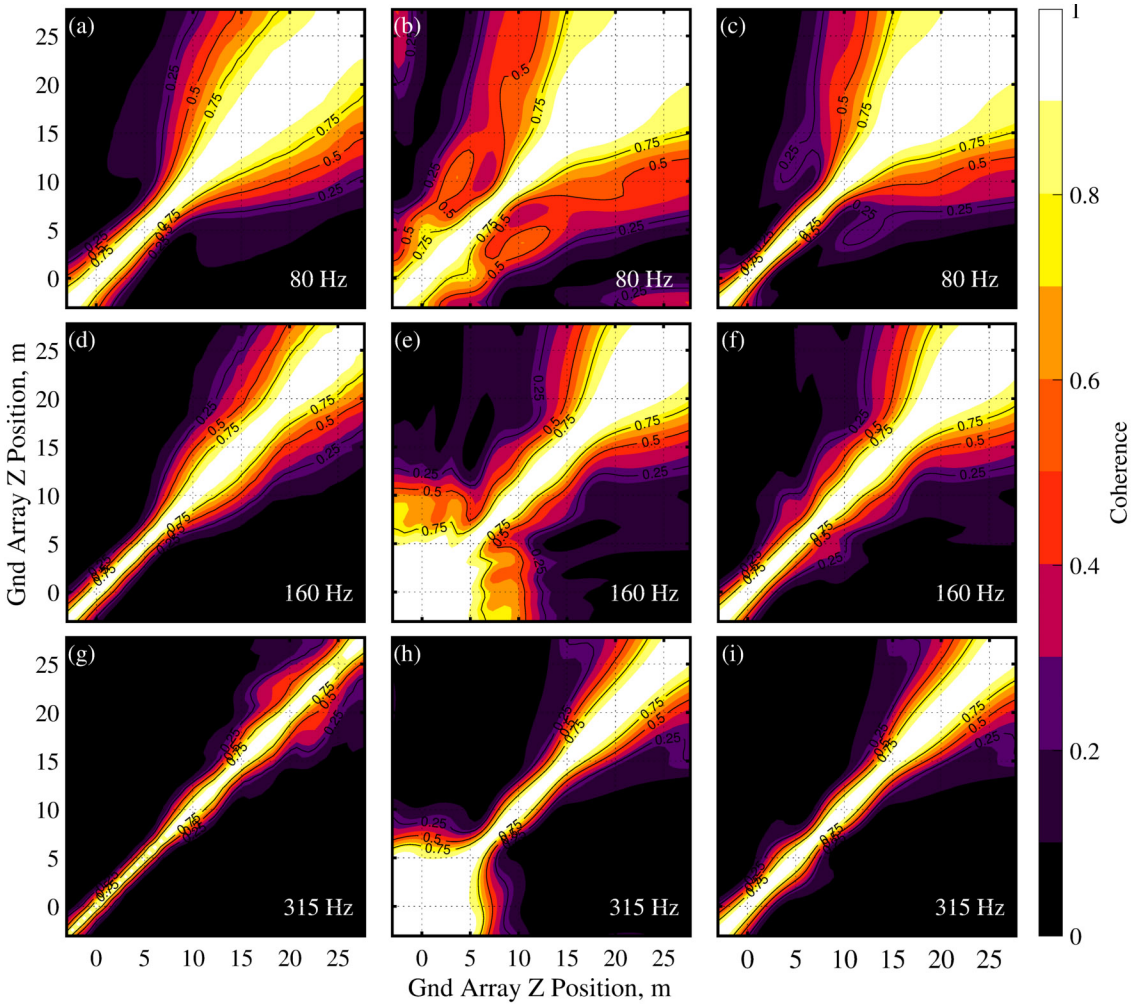

Fig. 10. Measured Coherence at the ground array for (a) 80, (d) 160, and (g) 315 Hz. The predicted coherence using the multiple-wavepacket source-model is shown for (b) 80, (e) 160, and (h) 315 Hz. In addition, the predicted coherence from the multiple-wavepacket model and uncorrelated distribution is shown for (c) 80, (f) 160, and (i) 315 Hz.

The coherence is estimated at each of these frequencies using both the MWP and the MWP+UD reduced-order models. In the case of coherence estimated by the MWP model, the qualitative features found in the measured coherence maps are present for measurements where $Z \geq 5$ m. However, the coherence features are generally overestimated, and the coherence predictions for $Z < 5$ m are greatly overestimated and bear no resemeblance to the measured coherence. While additional wavepackets reduce the overestimation of the coherence in most regions across the measurement array, a large number of wavepackets is required to adequately reproduce the short coherence lengths to the sideline, likely resulting from the fine-scale structure radiation seen by Neilsen *et al.*[31] The MWP+UD model incorporates the additional distributed uncorrelated source and the predicted coherence, shown in the right column of Fig. 10, corrects the overestimated coherence, particularly for the sideline predictions, and also reduces the

Downloaded by BRIGHAM YOUNG UNIVERSITY on June 8, 2017 | http://arc.aiaa.org | DOI: 10.2514/6.2017-4048

overestimation of the coherence farther downstream along the measurement array. The inclusion of both directive wavepackets and an uncorrelated distribution allows for the accurate prediction of coherence properties both to the sideline and within the maximum radiation region where large-scale structure radiation is present. The need for the distinctive source components qualitatively supports the theory of two distinct source mechanisms.[31, 39]

E. Optimizing the Wavepacket Model

In the preceding analyses, six wavepackets were chosen as a preliminary choice for the MWP and MWP+UD models, regardless of frequency. This is not necessarily the optimal number of wavepackets, as fewer wavepackets can be used to accurately describe the radiation, particularly at lower frequencies whereas additional wavepackets are required with increasing frequency. To gain a sense of the required number of wavepackets for each frequency, the decibel level differences—shown in Fig. 6(d) for the measurement arc—are averaged for each frequency between measurements at both the scanning array and the arc and the predicted levels from the MWP model. The errors between the MWP model and both field array measurements are calculated for a variable number of included wavepackets, from one to ten, and the average errors are shown in Fig. 11(a-b) for the scan array and the measurement arc, respectively. In these plots, the horizontal axis shows the number of wavepackets used in the multiple-wavepacket model for a given frequency and the colored contour lines provide the average error of the model. In addition, the average error of the equivalent source model from the beamforming results is shown at the far right of each plot. It is assumed that in the limit of adding multiple wavepackets, the errors will converge to those of the beamforming model. From the results, it is shown that by using six wavepackets, the average level errors at the scan array are between 2-3 dB at all frequencies, and some frequencies, and as few as one wavepacket will describe radiation to within about 3 dB on average for frequencies below 125 Hz, although additional wavepackets are required for higher frequencies. At the measurement arc, which is located slightly farther downstream from the sideline, additional wavepackets are required to accurately predict the radiation levels, and errors increase with frequency unless at least five wavepackets are used.

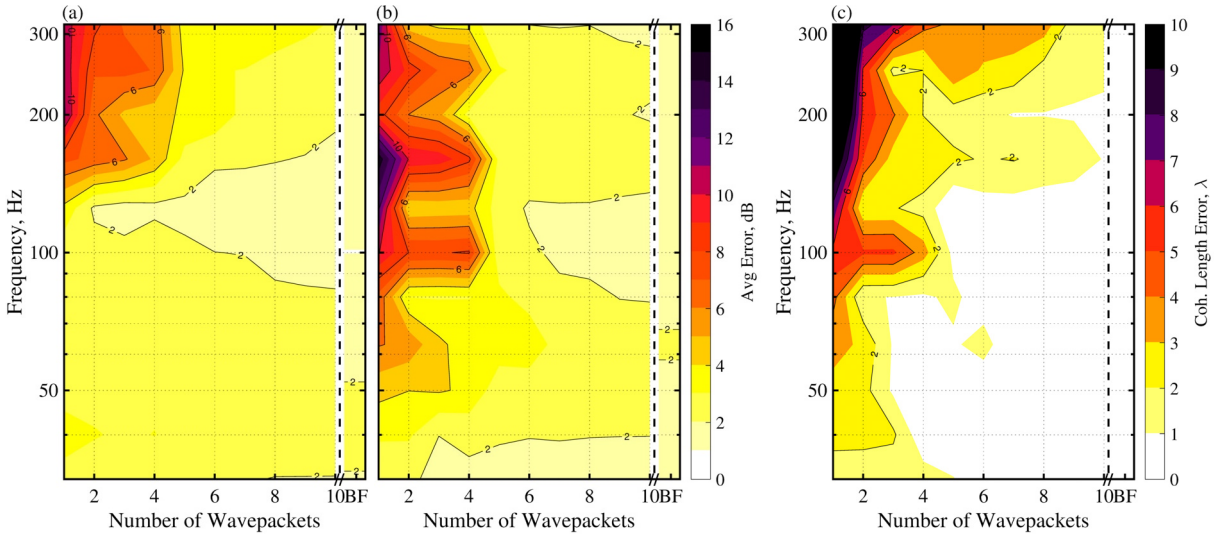

Fig. 11. Average Error of predicted levels from wavepacket models to (a) the scanning array measurements and (b) the arc measurements. (c) The error, in wavelengths, of coherence length from wavepacket models and beamforming results to coherence measurements at the ground array. The coherence is measured about the position of maximum level at the array. In each plot, the predicted levels and coherence length errors for each respective data of the beamforming results is plotted to the far right.

The predictions of the field coherence using the MWP model are also affected by the included number of wavepackets as too few overestimates the coherence values as shown in Fig. 10. To compare the capability of the MWP model to predict the coherence properties of the field, the coherence length measured at the ground array is compared to the predicted coherence length from the wavepacket model. The coherence length, L_{γ^2}, is determined by taking the distance over which the coherence, referenced to a given location, is greater than 0.5.[40] Coherence lengths are calculated for every microphone reference position along the measurement array. The average error of the

Downloaded by BRIGHAM YOUNG UNIVERSITY on June 8, 2017 | http://arc.aiaa.org | DOI: 10.2514/6.2017-4048

coherence lengths, in wavelengths, is plotted as a function of the number of wavepackets used in the wavepacket model in Fig. 11(c). Because coherence is necessarily infinite when only one wavepacket is used, the limiting average error of the coherence lengths is shown for the case of one wavepacket. Errors for a MWP model of six wavepackets are less than two wavelengths for frequencies less than about 200 Hz, with additional wavepackets improving the coherence error. Like the level-based estimates, fewer wavepackets are required to predict the coherence properties for lower frequencies, and additional wavepackets improve the average coherence error primarily for coherence predictions to the sideline.

The error plots previously described result from MWP model estimations of the radiation levels and coherence properties. As shown in Fig. 5, the majority of the error in estimates of the acoustic radiation from the MWP model are at low directivity angles to the sideline of the jet, while the main lobe and large amplitude features are well represented by wavepacket systems. The combination wavepacket model and uncorrelated distribution (WPKT+UD) was used to estimate the levels at the scan plane and the arc, and the average errors of those level estimates to the measurements are shown in Fig. 12(a-b), respectively. Like Fig. 11(a-b), the horizontal axis shows the chosen number of wavepackets, and the level of the uncorrelated distribution was adjusted for each case to best match the sideline levels at the measurement array. The inclusion of the uncorrelated distribution reduces errors at all frequency bands, although the reductions are most pronounced for models that include fewer than five wavepackets. For frequencies below 100 Hz, the average level error at the scan array is unchanged with the inclusion of the uncorrelated distribution, regardless of the number of wavepackets used. However, errors below 100 Hz at the measurement arc show the need for at least five wavepackets before errors approach limiting values. The uncorrelated distribution also dramatically reduces the average error for frequencies above 100 Hz so that level errors using four wavepackets fall by nearly 3 dB. The estimates of coherence length at the ground array were also made using the WPKT+UD model, and the coherence length error, in wavelengths, of the estimated coherence lengths to the measurements are shown in Fig. 12(c). When compared to Fig. 11(c), the coherence length measurements are significantly improved by the inclusion of the uncorrelated distribution, particularly for models that include fewer than four wavepackets, and the effects are mostly noticeable when using between 1-3 wavepackets in the wavepacket model. Here, the improvements to the coherence predictions from those made using the MWP model alone are pronounced because of the improved coherence length predictions to the jet sideline where the fine-scale structure radiation is prevalent.[10]

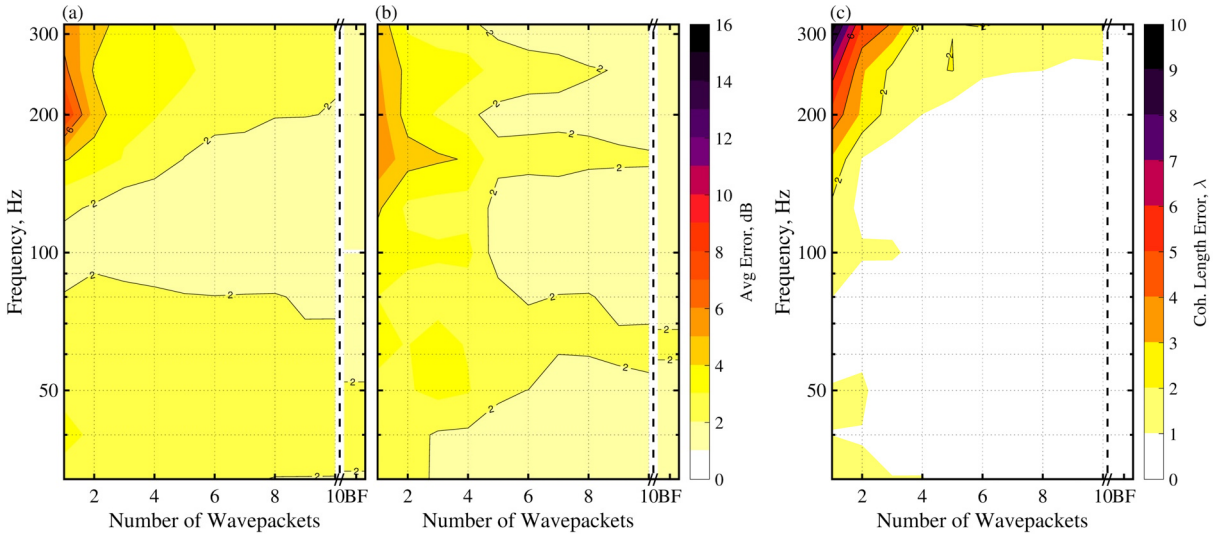

Fig. 12. Average Error of predicted levels from wavepacket models with an additional uncorrelated distribution to (a) the scanning array measurements and (b) the arc measurements. (c) The error, in wavelengths, of coherence length from wavepacket models with the additional uncorrelated distribution to coherence measurements at the ground array.

F. Engine Condition Analysis

Previous results were shown for MIL engine condition (100% engine thrust request [ETR]). In addition to this condition, both intermediate (INTER; ~25% ETR) and afterburner (AB; 150% ETR) conditions were measured at the ground array, scan array and measurement arc. The variation in temperature and jet velocity necessitates additional

Downloaded by BRIGHAM YOUNG UNIVERSITY on June 8, 2017 | http://arc.aiaa.org | DOI: 10.2514/6.2017-4048

consideration for the MWP models, and it provides additional insights into the source and radiation properties. The multiple-wavepacket modeling of the equivalent beamforming results can also lend insight into sources' coherence and radiation properties.

Beamforming equivalent source results are shown in Fig. 13 for INTER and AB engine conditions with levels given relative to the respective maximum level of each frequency. Both engines show similar general trends seen in the MIL engine condition with some important distinctions. At INTER, the maximum levels of the beamforming results are shifted about 2-3 m upstream of the MIL results, while the peak levels at AB are about 1-2 m farther downstream. Additionally, the source width for INTER shows a smaller source width across the frequency range as measured from the 3 dB down contour lines (between 1.5-2.5 wavelengths when scaled). The largest deviations, however, occur in the coherence length measurements shown by the red dashed lines overlaid on the beamforming results. They indicate that while coherence lengths are marginally less at INTER for frequencies above 160 Hz, they are much less for frequencies below a 160 Hz when compared to the MIL results. For example, at 50 Hz, $L_{\gamma^2} = 7.8$ m at INTER and $L_{\gamma^2} = 27.2$ m at MIL even though the difference in source size is only about 4 m as measured from the 12 dB down lines of the beamforming results. When scaled, the coherence lengths are very consistent across the frequency range with a length of about one wavelength everywhere except at 80 Hz where the length is about two wavelengths. Neilsen *et al.*[31] showed that, according to ground array data for INTER engine condition, the relative contribution in level of the fine- and large-scale structure radiation to the measured spectra are within a few dB of each other between for radiated angles of $80 - 120°$, whereas the relative differences in level of the two spectra are much greater at MIL and AB conditions. The combination of the two sources within the source region that have relatively equal levels may explain the small coherence lengths at INTER for frequencies below 160 Hz. It should also be noted that the maximum radiation region at INTER extends slightly beyond the measurement array (see Ref. [30]) for frequencies below about 160 Hz, thus, a portion of the radiation information is not adequately represented and the INTER coherence lengths below 160 Hz may be larger than shown in Fig. 13(a). The levels and coherence properties of the beamforming results at AB condition only show minor differences from those at MIL. The source widths between MIL and AB vary only 1-2 m across the frequency as measured by the 3 dB down contour lines, although the effect is most pronounced for frequencies above 125 Hz because the source width at AB shows much less contraction with increasing frequency above 100 Hz. The coherence lengths are mostly similar between MIL and AB, except that the coherence lengths between 100-200 Hz are slightly larger at MIL condition than at AB.

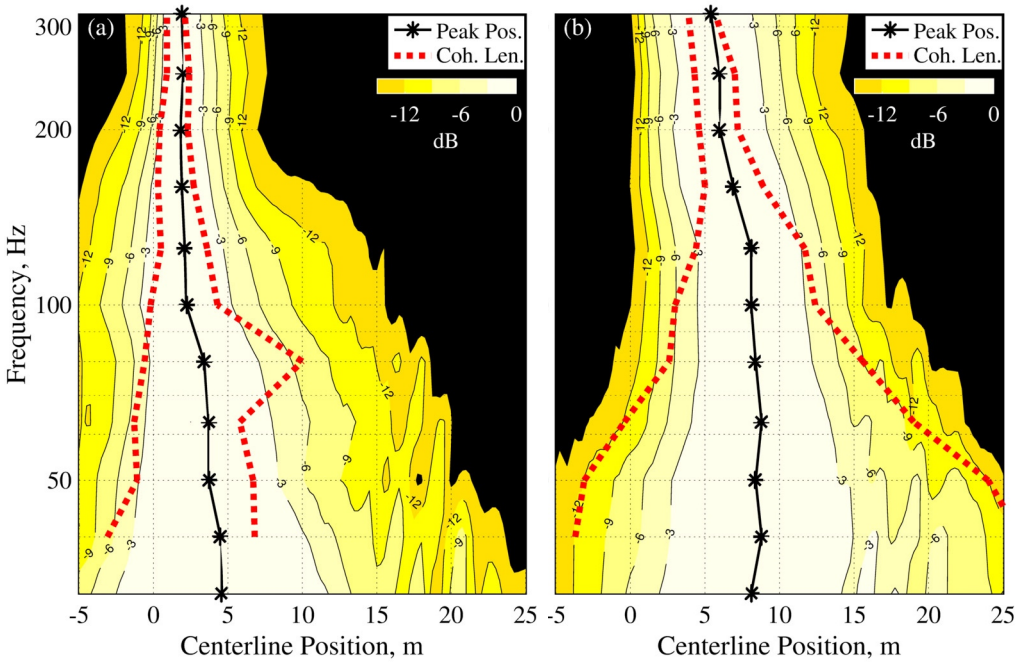

Fig. 13. One-third octave beamforming results at jet centerline shown relative to the maximum level of each frequency, for (a) INTER and (b) AB engine conditions. The location of the maximum level at each frequency

Downloaded by BRIGHAM YOUNG UNIVERSITY on June 8, 2017 | http://arc.aiaa.org | DOI: 10.2514/6.2017-4048

is indicated with an asterisk, and the coherence region over which coherence exceeds 0.5 relative to the peak beamforming level location is also delineated with a red dashed line.

The MWP decompositions are performed on the beamforming results shown in Fig. 13, for example frequencies at 315 Hz, 160 Hz and 80 Hz in Fig. 14. For a given frequency, the amplitude contribution of each wavepacket does not vary significantly with engine condition, although the change in the beamforming source width and coherence lengths with frequency and engine condition produce significant differences in the MWP models. At 315 Hz, the difference in source width is pronounced between INTER and AB conditions, with the INTER condition showing a very tightly packed set of overlapping wavepackets, and wavepackets in the AB condition more evenly distributed across the larger source distribution. Thus, while coherence lengths shown in Fig. 13 are only about 0.5 m larger at AB compared to INTER at 315 Hz, the source width is about 3 m larger. At 160 Hz, individual wavepacket contributions are more evenly spread compared to the examples at 315 Hz. The source width for AB is very similar between 160 Hz and 80 Hz, with the greatest difference being the smaller coherence lengths at 160 Hz necessitate a larger number of wavepackets dispersed throughout the source distribution, whereas one primary wavepacket constitutes most of the radiation at 80 Hz. In fact, one wavepacket captures most of the amplitude for all three engine conditions at this frequency. When normalized and scaled by wavelength the differences of the primary wavepackets in both engine conditions are not pronounced, although the trend is to grow slightly in width with increasing frequency.

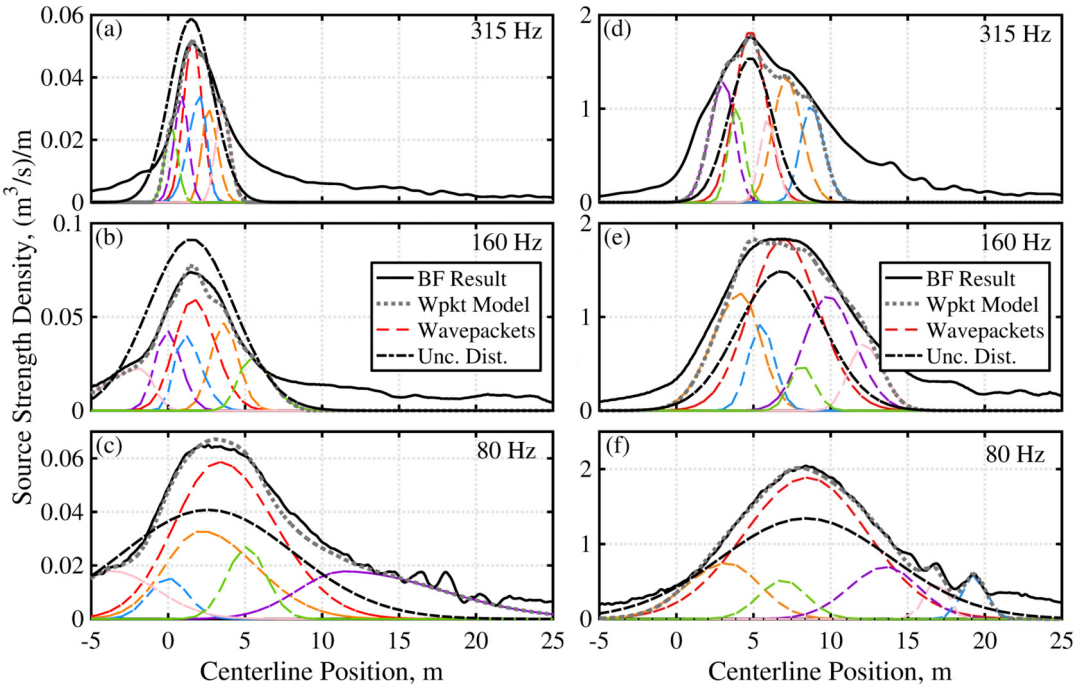

Fig. 14. Wavepacket examples at (a) 315 Hz, (b) 160 Hz, and (c) 80 Hz using six wavepackets are shown with the beamforming and resultant wavepacket model levels for (left) INTER and (right) AB engine conditions.

In addition to the MWP models, the uncorrelated distribution is also overlaid on each plot using dash-dot lines. Like the uncorrelated distribution at the MIL condition, the width of each is three wavelengths measured at the full-width half maximum. The amplitude of each distribution varies with engine and frequency, and in some cases the distribution amplitude exceeds the amplitude of the beamforming results. Because uncorrelated distributions do not radiate coherently, the source amplitude required to accurately predict field levels is necessarily higher than for coherent sources.

The number of wavepackets required to generate an effective level-based MWP+UD model does not significantly vary with a change in engine condition, although accurate coherence prediction generally require a higher wavepacket count. While not shown here, similar trends seen in the MIL conditions are present at for the AB condition in that 4-6 wavepackets adequately predicts levels at the measurement arc with average errors less than 3 dB, and fewer can be incorporated at lower frequencies. Similarly, the average predicted level errors at the INTER condition approach a limiting value using as few as six wavepackets. However, while average errors in the predicted levels can provide

Downloaded by BRIGHAM YOUNG UNIVERSITY on June 8, 2017 | http://arc.aiaa.org | DOI: 10.2514/6.2017-4048

insight into the necessary number of wavepackets to describe the level radiation, the coherence lengths of the radiation in the field benchmark the spatiotemporal capabilities for the models. Similar to the MIL results of Fig. 12(c), as few as 4-6 wavepackets produce coherence length errors below $\pm 1\lambda$ for the AB condition across the frequency region of interest. However, at INTER, the inclusion of up to ten or more wavepackets is necessary to accurately predict the coherence lengths for frequencies above 125 Hz. Because the wavepackets constitute the majority of the radiation in the region of maximum levels along the measurement array, the inclusion of a large number of wavepackets and the tight spacing of the wavepackets within the source distribution at 315 Hz shown in Fig. 14 shows the highly uncorrelated nature of the jet noise source at INTER, even in the maximum radiation region.

The MWP and MWP+UD models are validated by predicting the levels at the ground array, scan array and measurement arc for INTER and AB conditions in Fig. 15 and Fig. 16. In each case, predicted levels match to within 2 dB for most regions with few exceptions. At 160 Hz and 315 Hz, the ground-based array measurements do not show indication of strong multilobe directivity patterns, and consequentially the scan array and arc array level predictions do not include multilobe radiation. Because of the INTER condition's high variability in the actual engine output from scan to scan along the measurement arc,[30] it is more difficult to accurately compare the predicted levels to the benchmark measurements. As a result, level predictions at the measurement arc in Fig. 15 show up to 5-10 dB errors for measurements at angles greater than 110°. However, the sideline radiation is more accurately captured with the six MWP model compared to similar models at MIL and AB conditions, suggesting that because less directive radiation is present at this condition, the MWP model placed higher emphasis on the sideline radiation. Errors at the sideline, particularly for the ground array, are much greater at the AB condition in Fig. 16 with deviation up to 15 dB for the MWP model. The MWP+UD model boosts the sideline radiation and shows agreement to within 1-2 dB with most measurements at the scan and arc arrays. These predicted levels show that for multiple engine conditions and radiation angles, the MWP model predicts the INTER condition radiation as well as the large-scale structure radiation at AB condition using a relatively few number of sources, and the addition of an uncorrelated distribution allows for the accurate prediction of the sideline levels as well.

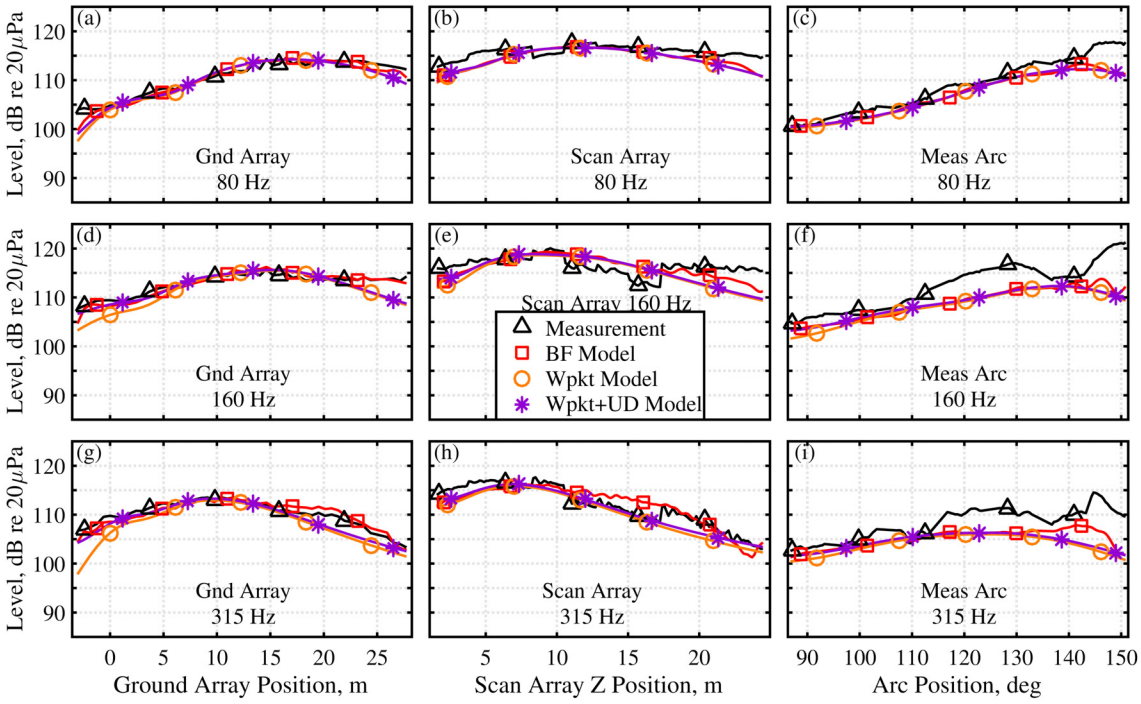

Fig. 15. Comparisons of measurements and predicted levels for (a-c) 80 Hz and (d-f) 160 Hz at (left) the ground array, (middle) the scan array, and (right) the measurement arc, at INTER engine condition (Compare with Fig. 5).

Downloaded by BRIGHAM YOUNG UNIVERSITY on June 8, 2017 | http://arc.aiaa.org | DOI: 10.2514/6.2017-4048

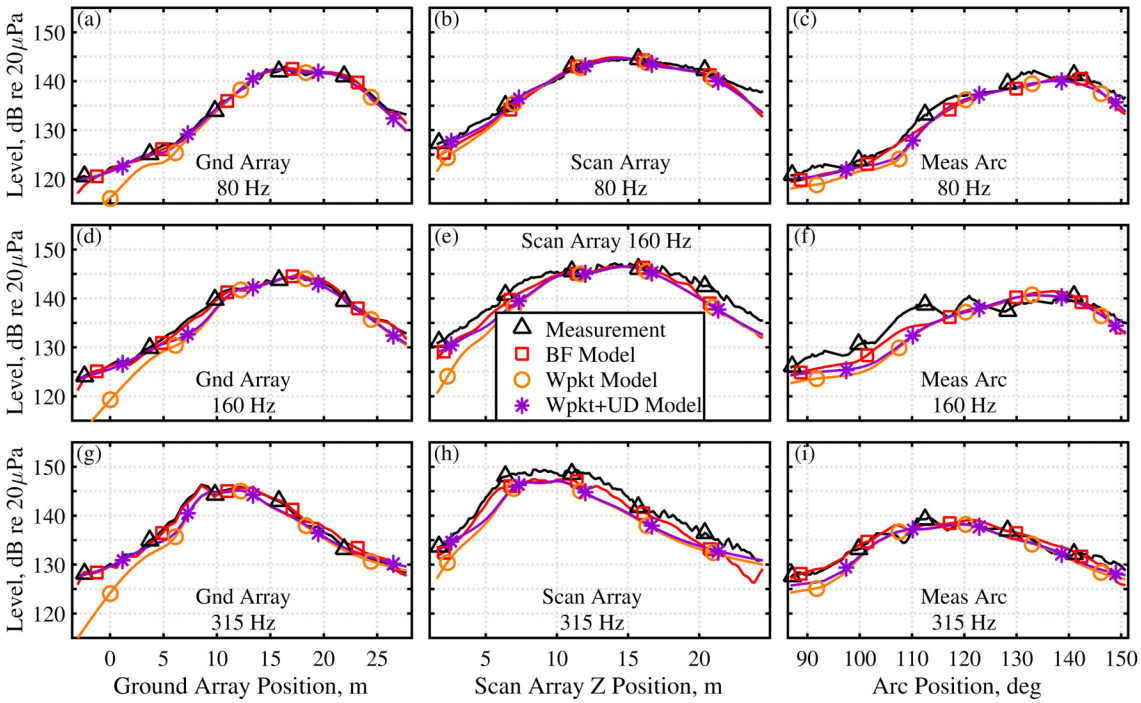

Fig. 16. Similar to Fig. 15 for AB engine condition.

The MWP+UD model, having been verified to accurately predict levels to within 2 dB at the three measured arrays—insofar as permitted by the beamforming model predictions—is now used to predict the radiation beyond measured locations. The predicted levels are shown in Fig. 17 for INTER, MIL and AB engine conditions using the MWP+UD model for frequencies of 80 Hz, 160 Hz and 315 Hz. With example frequencies at each of the engine conditions, a comparison of the radiation using the predicted levels using the MWP+UD model can be made. The general trends show that the maximum radiation angles smaller with increasing engine condition, regardless of frequency. For example, at 80 Hz, the directivity angle of the primary wavepacket shifts from 136° at INTER to 125° at AB. In addition, the radiation becomes more directive with increasing condition, which may be a direct consequence of the greater relative contribution from large-scale structure radiation.[31] There are also frequency-specific differences in the radiation. At 160 Hz, the transition from a single lobe to multilobe radiation occurs between the INTER and MIL cases, and at AB the radiation shows small signs of multilobe radiation albeit much less pronounced. The same multilobe effects are present at 315 Hz for the different engine conditions. At 160 Hz, indications of a secondary radiating lobe are present in the INTER and AB conditions, although the differences in the directivities of the two lobes are less distinct. While the distinct peaks are not separable in the example frequencies shown in Fig. 15 and Fig. 16, the presence of distinct lobes are confirmed in the spectral plots of the ground array measurements in Ref. [28]. Indications of the double lobe in the INTER condition support the theory that higher temperature and engine conditions at MIL and AB are not required to produce the double lobe phenomena, and the differences in radiation angle of the lobes are greatest at MIL rather than at AB. Tam *et al.*[41] hypothesized that the double lobe phenomenon was the result of both large-scale radiation and combustion noise. However, while high engine powers exhibit strong effects due to combustion noise—which should radiate from the nozzle exit—the multilobe directivity pattern is present at lower engine powers. Additionally, beamforming and MWP model decompositions reveal that both radiation lobes seem originate many meters further downstream from the nozzle exit.

Downloaded by BRIGHAM YOUNG UNIVERSITY on June 8, 2017 | http://arc.aiaa.org | DOI: 10.2514/6.2017-4048

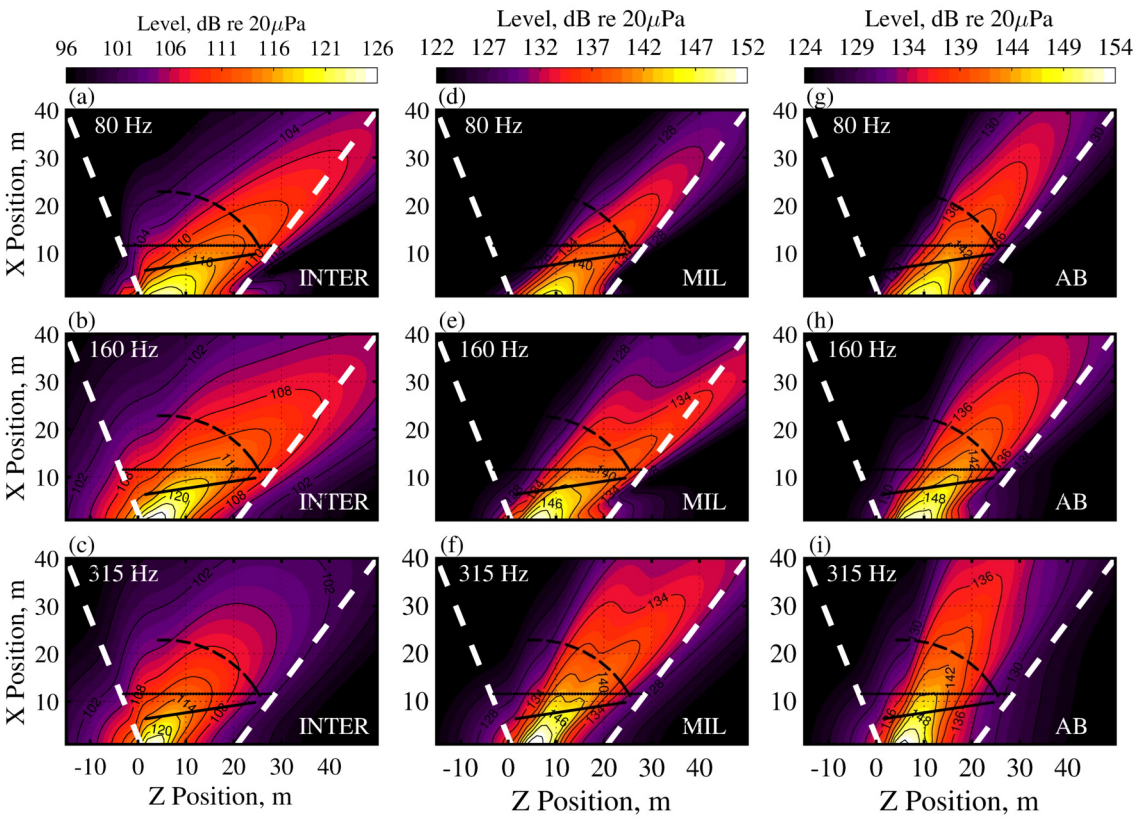

Fig. 17. Predicted levels across a horizontal plane with jet centerline on Z axis. Cases for (top) 80 Hz, (middle) 160 Hz, and (bottom) 315 Hz are shown using a multiple-wavepacket model with an additional monopole distribution for (a-c) INTER, (d-f) MIL, and (g-i) AB engine conditions.

IV. Conclusion

Multiple-wavepacket source models of the noise radiation from a high-performance tactical aircraft operating at MIL engine condition are developed using a decomposition of phased-array source reconstructions. The investigation builds on beamforming investigations that focus on source distributions as a function of frequency derived using improved generalized inverse beamforming. The beamforming results show a strong distributed source region that radiates most efficiently at frequencies above 100 Hz. This beamforming-derived equivalent source region extends multiple meters, and the source width contracts and moves towards the engine nozzle exit with increasing frequency, consistent with comparable laboratory-scale measurements. However, when scaled by wavelength, the width of the source distribution region nearly triples over an octave frequency band. Interestingly, the coherence lengths across the beamforming source distribution shrink (as a function of wavelength) with increasing frequency. The inverse relationship between the source width and the coherence length scales suggests that additional partially-correlated sources are required to appropriately model the source distribution as frequency is increased.

The beamforming source is decomposed into a multiple-wavepacket (MWP) model consisting of six asymmetric-Gaussian-shaped wavepackets, with each having a distinct phase speed. This MWP model allows for the prediction of level-based radiation as well as coherence properties of the field where single wavepacket models fail. In addition, the MWP model can be augmented by an uncorrelated distribution (MWP+UD) to accurately predict levels where fine-scale structure radiation dominates. These models are validated using benchmark level and coherence measurements at various distances and angles the mid field. Average errors for the MWP model are between 2-3 dB, and errors drop to 1-2 dB when the MWP+UD model is used. This is particularly due to the inability of the MWP model to capture the sideline radiation, which would otherwise require a significant number of wavepackets. The average errors of the predicted coherence lengths in the mid field are about 1-2 wavelengths for frequencies below 200 Hz using the MWP model and coherence lengths to the sideline are improved further using the MWP+UD model.

The MWP models are used to predict level and coherence properties across a usable aperture, defined by the measurement array used in the beamforming analysis. The results are shown alongside the predicted beamforming results, and the predicted levels using the reduced-order models show consistency with the full-order beamforming

Downloaded by BRIGHAM YOUNG UNIVERSITY on June 8, 2017 | http://arc.aiaa.org | DOI: 10.2514/6.2017-4048

predictions. The predicted levels show that multilobe directivity patterns are apparent in the jet noise at 160 Hz and 315 Hz for the MIL condition, and that with increasing frequency the relative levels between the lobes shift so that the upstream lobes grow in level while the downstream lobes decrease. When the radiation of each contributing wavepacket is viewed separately, the multilobe radiation is reducible into two wavepackets, and the remaining wavepackets are necessary to reconstruct any residual energy. Reproduction of the multilobe directivity using the MWP model shows that overlapping sources with differing phase speeds can effectively generate multilobe radiation patterns.

An analysis of the primary wavepacket from the MWP model shows a high degree of similarity across the frequency range once normalized and scaled by the wavelength. This result, combined with the finding that the source size grows with increasing frequency, suggests that the relative importance of the nonprimary wavepackets increases with frequency and that the combination of these wavepackets, when spatially distributed, comprise the source distribution. In addition, the primary wavepackets, which are connected to the primary radiation directivity, show a smooth transition in directivity to larger angles relative to the nozzle inlet from 32 Hz to 160 Hz, a trend which has not previously been noted for mixing noise radiation in the literature. At 160 Hz the directivity of the primary wavepacket transitions to the more upstream lobe of the multilobe radiation, and thereafter the directivity slowly increases to larger angles with increasing frequency—albeit smaller than those of the more downstream radiation lobe.

An optimization study was also performed to determine the necessary number of wavepackets required to accurately predict the radiation and coherence properties of the field. While the addition of wavepackets reduces the error between measurements and predicted levels, these errors converge on limiting values of between 1-3 dB, dependent on frequency. The MWP shows level-based average errors on the order of 2-3 dB when using six wavepackets across the analyzed frequency range at both the scan array and measurement arc, and coherence errors fall to within two wavelengths for frequencies below 200 Hz using a six wavepacket MWP model. However, when the uncorrelated distribution is included, as few as one wavepacket is sufficient to predict radiation levels to within 1-3 dB for frequencies below 125 Hz, while 4-6 are needed above 200 Hz to produce similar errors. The coherence errors using the MWP+UD model are also reduced, and when four wavepackets are included in the model the errors fall to within one wavelength below 200 Hz.

Additionally, the INTER and AB engine conditions were analyzed and MWP models produced to predict the radiation properties. The beamforming results showed that the source width was relatively constant across the frequency range at INTER with a width of about two wavelengths, as measured from 3 dB of the peak levels, while the source width grows with increasing frequency (as a function of wavelength) at AB, like results at MIL. The source coherence lengths, however, were much smaller at INTER for frequencies below 160 Hz presumably due to the relatively larger contribution of fine-scale structure radiation that competes with the large-scale structure radiation levels. When decomposed into the MWP models using six wavepackets, the variation between the INTER and AB results led to more dispersed wavepackets across the source in the AB case and more densely-spaced overlapping wavepackets at INTER. The MWP models were again successfully validated using benchmark measurements to show that, regardless of engine condition, a reduced order model of the jet noise was successfully obtained. The MWP model again produced average errors within 1-3 dB within the large-scale structure radiation regions, and the addition of the uncorrelated distribution allowed for accurate level predictions in regions dominated by the fine-scale structure radiation.

The ability of the MWP and MWP+UD models to efficiently and effectively predict the noise environment near high-performance tactical aircraft is a significant cost-reducing achievement by requiring fewer measurements and acquisition resources. Analytical functions that produce a reduced-order source model provide a modular and scalable framework that can be used to compare with other measurements. In addition, the model's analytical framework allows for future work to create a broadband analytical MWP model for a more complete picture of the radiated properties beyond limits imposed by measurement array geometry. The model is also important in its ability to reproduce the more intricate features of the radiation, including the multilobe directivity patterns found in tactical aircraft measurements. Building on the successes of previous wavepacket models, the ability of the MWP model to predict coherence properties brings analytical modeling efforts closer to physical properties of the radiation. Time-domain intermittency and impulses have not been considered in the present work, and it is hypothesized that future efforts to incorporate additional physical properties of the jet noise into a reduced-order analytical framework will provide better predictive capabilities for time domain events. This is particularly true for future efforts to improve upon the far-field capabilities of the MWP model, particularly when nonlinear propagation is present, to provide a more complete model to globally predict the radiation properties.

Downloaded by BRIGHAM YOUNG UNIVERSITY on June 8, 2017 | http://arc.aiaa.org | DOI: 10.2514/6.2017-4048

V. Acknowledgments

The authors gratefully acknowledge the funding for this analysis from the Office of Naval Research. The measurements were funded by the U.S. Air Force Research Laboratory (USAFRL) through the Small Business Innovation Research program, and supported through a cooperative research and development agreement between Blue Ridge Research and Consulting, Brigham Young University, and the U.S. Air Force. This research was supported in part by the appointment of Blaine Harker to the Student Research Participation Program at USAFRL, 711th Human Performance Wing, Human Effectiveness Directorate, Warfighter Interface Branch, Battlespace Acoustics Branch administered by the Oak Ridge Institute for Science and Education through an interagency agreement between the U.S. Department of Energy and USAFRL.

DISTRIBUTION STATEMENT A. Approved for public release: distribution is unlimited. 88ABW Cleared 04/24/017; 88ABW-2017-1908.

VI. References

[1]T. Suzuki and T. Colonius, "Instability waves in a subsonic round jet detected using a near-field phased microphone array," *Journal of Fluid Mechanics* **565**, 197-226 (2006).

[2]D. Papamoschou, P. J. Morris, and D. K. McLaughlin, "Beamformed flow-acoustic correlations in high-speed jets," AIAA Paper 2009-3212, 2009.

[3]R. Reba, S. Narayanan, and T. Colonius, "Wave-packet models for large-scale mixing noise," *International Journal of Aeroacoustics* **9**, 533-558 (2010).

[4]M. Koenig, A. V. Cavalieri, P. Jordan, J. Delville, Y. Gervais, and D. Papamoschou, "Farfield filtering and source imaging of subsonic jet noise," *Journal of Sound and Vibration* **332**, 4067-4088 (2013).

[5]P. Jordan and T. Colonius, "Wave packets and turbulent jet noise," *Annual Review of Fluid Mechanics* **45**, 173-195 (2013).

[6]R. Schlinker, S. Liljenberg, D. Polak, K. Post, C. Chipman, and A. Stern, "Supersonic Jet Noise Source Characteristics & Propagation: Engine and Model Scale," AIAA Paper 2007-3623, 2007.

[7]R. Dougherty and J. Mendoza, "Phased Array Beamforming with 100-Foot Polar Arc Microphones in a Static Engine Noise Test," AIAA Paper 2008-51, 2008.

[8]T. F. Brooks, W. M. Humphreys, and G. E. Plassman, "DAMAS Processing for a Phased Array Study in the NASA Langley Jet Noise Laboratory," AIAA Paper 2010-3780, 2010.

[9]S. S. Lee and J. Bridges, "Phased-Array Study of Dual-Flow Jet Noise: Effect of Nozzles and Mixers," AIAA Paper 2006-2647, 2006.

[10]C. K. W. Tam, K. Viswanathan, K. K. Ahuja, and J. Panda, "The sources of jet noise: Experimental evidence," *Journal of Fluid Mechanics* **615**, 253-292 (2008).

[11]R. P. Dougherty, "Improved generalized inverse beamforming for jet noise," *International Journal of Aeroacoustics* **11**, 259-290 (2012).

[12]S. R. Venkatesh, D. R. Polak, and S. Narayanan, "Beamforming algorithm for distributed source localization and its application to jet noise," *AIAA Journal* **41**, 1238-1246 (2003).

[13]T. F. Brooks and W. M. Humphreys, "A deconvolution approach for the mapping of acoustic sources (DAMAS) determined from phased microphone arrays," *Journal of Sound and Vibration* **294**, 856-879 (2006).

[14]T. F. Brooks and W. M. Humphreys Jr, "Extension of DAMAS phased array processing for spatial coherence determination (DAMAS-C)," AIAA Paper 2006-2654, 2006.

[15]U. Michel and S. Funke, "Noise source analysis of an aeroengine with a new inverse method SODIX," AIAA Paper 2008-2860, 2008.

[16]D. Papamoschou, "Wavepacket modeling of the jet noise source," AIAA Paper 2011-2835, 2011.

[17]T. Padois, A. Berry, P.-A. Gauthier, and N. Joshi, "Beamforming matrix regularization and inverse problem for sound source localization : application to aero-engine noise," AIAA Paper 2013-2212, 2013.

[18]T. Suzuki, "L1 generalized inverse beam-forming algorithm resolving coherent/incoherent, distributed and multipole sources," *Journal of Sound and Vibration* **330**, 5835-5851 (2011).

[19]Y. Du and J. M. Philip, "Numerical simulation of the effect of a low bypass cooling stream on supersonic jet noise," AIAA Paper 2014-1402, 2014.

[20]B. M. Harker, K. L. Gee, T. B. Neilsen, A. T. Wall, and M. M. James, "Wavepacket modeling and fullscale military jet noise beamforming analyses," AIAA Paper 2016-2129, 2016.

[21]A. T. Wall, K. L. Gee, T. B. Neilsen, B. M. Harker, S. A. McInerny, R. C. McKinley, and M. M. James, "Investigation of multi-lobed fighter jet noise sources using acoustical holography and partial field decomposition methods," AIAA Paper 2015-2379, 2015.

[22]R. P. Dougherty, "Beamforming in acoustic testing," *Experimental Fluid Mechanics Series, Berlin, Germany, Springer-Verlag GmbH, 200*262-97 (2002).

[23]E. Sarradj, "Three-Dimensional Acoustic Source Mapping with Different Beamforming Steering Vector Formulations," *Advances in Acoustics and Vibration* **2012**, (2012).

Downloaded by BRIGHAM YOUNG UNIVERSITY on June 8, 2017 | http://arc.aiaa.org | DOI: 10.2514/6.2017-4048

[24]A. T. Wall, "The characterization of military aircraft jet noise using near-field acoustical holography methods," Dissertation, Brigham Young University, 2013.
[25]R. Schmidt, "Multiple emitter location and signal parameter estimation," *IEEE transactions on antennas and propagation* **34**, 276-280 (1986).
[26]S. Hassani, *Mathematical physics: a modern introduction to its foundations*. (Springer Science & Business Media, 2013), pp. 33-35
[27]E. G. Williams, "Regularization methods for near-field acoustical holography," *The Journal of the Acoustical Society of America* **110**, 1976-1988 (2001).
[28]B. M. Harker, T. B. Neilsen, K. L. Gee, A. T. Wall, and M. M. James, "Spatiotemporal Correlation Analysis of Jet Noise from a High-Performance Military Aircraft," *AIAA Journal* **54**, 1554-1566 (2016).
[29]A. T. Wall, M. D. Gardner, K. L. Gee, and T. B. Neilsen, "Coherence length as a figure of merit in multireference near-field acoustical holographya)," *The Journal of the Acoustical Society of America* **132**, EL215-EL221 (2012).
[30]A. T. Wall, K. L. Gee, M. M. James, K. A. Bradley, S. A. McInerny, and T. B. Neilsen, "Near-field noise measurements of a high-performance military jet aircraft," *Noise Control Engineering Journal* **60**, 421-434 (2012).
[31]T. B. Neilsen, K. L. Gee, A. T. Wall, and M. M. James, "Similarity spectra analysis of high-performance jet aircraft noise," *Journal of the Acoustical Society of America* **133**, 2116-2125 (2013).
[32]J. Liu, A. T. Corrigan, K. Kailasanath, and E. J. Gutmark, "Effects of Temperature on Noise Generation in Supersonic Jets," AIAA Paper 2016-2937, 2016.
[33]J. P. Erwin, P. Panickar, P. Vogel, and N. Sinha, "Acoustic Source Localization of Rectangular Jets using Large Eddy Simulation with Numerical Phased Arrays," AIAA Paper 2014-0179, 2014.
[34]S. S. Lee and J. Bridges, "Phased-Array Measurements of Single Flow Hot Jets," AIAA Paper 2005-2842, 2005.
[35]T. A. Stout, K. L. Gee, T. B. Neilsen, A. T. Wall, and M. M. James, "Source characterization of full-scale jet noise using acoustic intensity," *Noise Control Engineering Journal* **63**, 522-536 (2015).
[36]A. T. Wall, K. L. Gee, T. B. Neilsen, R. L. McKinley, and M. M. James, "Military jet noise source imaging using multisource statistically optimized near-field acoustical holography," *The Journal of the Acoustical Society of America* **139**, 1938-1950 (2016).
[37]R. Reba, J. Simonich, and R. Schlinker, "Sound radiated by large-scale wave-packets in subsonic and supersonic jets," AIAA Paper 2009-3256, 2009.
[38]A. T. Wall, K. M. Leete, K. L. Gee, T. B. Neilsen, M. M. James, and R. L. McKinley, "Preliminary Investigation of Multiple Fighter Jet Noise Sources Using Acoustical Holography," Proceedings of 23rd AIAA/CEAS Aeroacoustics Conference (accepted), 2017.
[39]C. K. W. Tam, M. Golebiowski, and J. M. Seiner, "On the two components of turbulent mixing noise from supersonic jets," AIAA Paper 96-1716, 1996.
[40]A. T. Wall, M. D. Gardner, K. L. Gee, and T. B. Neilsen, "Coherence length as a figure of merit in multireference near-field acoustical holography," *Journal of the Acoustical Society of America* **132**, El215-El221 (2012).
[41]C. K. Tam and S. Parrish, "Noise of high-performance aircrafts at afterburner," AIAA Paper 2014-2754, 2014.

Downloaded by BRIGHAM YOUNG UNIVERSITY on June 8, 2017 | http://arc.aiaa.org | DOI: 10.2514/6.2017-4048